

University of South Alabama

JagWorks@USA

---

Theses and Dissertations

Graduate School

---

12-2023

## Examining the Efficacy of using IRT as an NDE method for CFRP and ZTCFRP Composites

William Wyatt Taylor

University of South Alabama, wyatttaylor1999@gmail.com

Follow this and additional works at: [https://jagworks.southalabama.edu/theses\\_diss](https://jagworks.southalabama.edu/theses_diss)



Part of the [Electro-Mechanical Systems Commons](#), and the [Other Mechanical Engineering Commons](#)

---

### Recommended Citation

Taylor, William Wyatt, "Examining the Efficacy of using IRT as an NDE method for CFRP and ZTCFRP Composites" (2023). *Theses and Dissertations*. 180.

[https://jagworks.southalabama.edu/theses\\_diss/180](https://jagworks.southalabama.edu/theses_diss/180)

This Thesis is brought to you for free and open access by the Graduate School at JagWorks@USA. It has been accepted for inclusion in Theses and Dissertations by an authorized administrator of JagWorks@USA. For more information, please contact [jherrmann@southalabama.edu](mailto:jherrmann@southalabama.edu).

THE UNIVERSITY OF SOUTH ALABAMA  
COLLEGE OF ENGINEERING

**NDE APPROACH USING IN-SITU JOULE HEATING THERMOGRAPHY FOR  
ADHESIVELY BONDED CFRP AND ZTCFRP COMPOSITE JOINTS**

BY

William W. Taylor

A Thesis

Submitted to the Graduate Faculty of the  
University of South Alabama  
in partial fulfillment of the  
requirements for the degree of

Master of Science



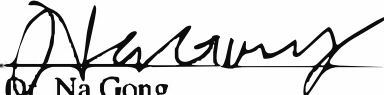
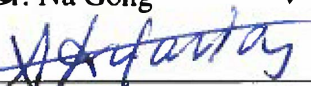
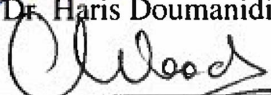

in

Mechanical Engineering

December 2023

Approved:

Date:

	<u>10-23-2023</u>
Chair of Thesis Committee: Dr. Kuang-Ting Hsiao	
	<u>10/23/2023</u>
Committee Member: Dr. Joseph D. Richardson	
	<u>10-23-2023</u>
Committee Member: Dr. Na Gong	
	<u>10/23/2023</u>
Chair of Department: Dr. Haris Domanidis	
	<u>October 23, 2023</u>
Director of Graduate Studies: Dr. Roger C. Woods	
	<u>11/9/2023</u>
Dean of the Graduate School: Dr. J. Harold Pardue	

**NDE APPROACH USING IN-SITU JOULE HEATING THERMOGRAPHY FOR  
ADHESIVELY BONDED CFRP AND ZTCFRP COMPOSITE JOINTS**

A Thesis

Submitted to the Graduate Faculty of the  
University of South Alabama  
in partial fulfillment of the  
requirements for the degree of

Master of Science

in

Mechanical Engineering

by

William W. Taylor

B.S., University of South Alabama, 2021

December 2023

## **ACKNOWLEDGEMENTS**

I want to thank my family for their support and guidance during my Masters study. I want to thank Dr. Hsiao, my research mentor, for his compassion and patience in escorting me to overcome challenges and keep up with research milestones. Furthermore, I want to sincerely thank him for showing me that my ambitions as a scholar are not without merit and for his help in how to be a better researcher and scientist. I am also thankful for the financial support from Dr. Hsiao's National Science Foundation grant (Award number: 2044513). I want to thank Dr. Richardson for his involvement in my committee and his down-to-earth approach to issues I have faced in both my bachelor and graduate studies. I want to thank Dr. Gong for her involvement in my committee and her patience and understanding. I want to thank my colleague Ryan Warren for his level-headed approach to tackling issues that appear in research, and his advice from his own experience during his Masters. I want to thank Rakibul Islam for his feedback in his Thesis as well. I want to thank the café staff at Shelby Hall for dispensing invigorating coffee for the last six years, which undoubtedly made late nights of work more manageable. I want to thank my friends, Ruthie Hill, Hannah Smith, Anna Hickman, Quinn Currie, Hayley Strickland, Melanie Lim, Liam Oswald, Georgia Robles, and many more for the support and understanding of the pressures of earning a Masters.

## TABLE OF CONTENTS

	Page
LIST OF TABLES .....	vi
LIST OF FIGURES .....	vii
LIST OF ABBREVIATIONS.....	xi
ABSTRACT.....	xii
CHAPTER I INTRODUCTION.....	1
1.1 Thesis hypotheses .....	2
1.1.1 Preliminary feasibility hypothesis.....	3
1.1.2 Improved investigational hypothesis .....	4
1.2 Thesis objectives.....	5
CHAPTER II LITERATURE REVIEW .....	7
2.1 NDE summary .....	7
2.1.1 Contact NDE methods .....	8
2.1.1.1 Electrical impedance tomography.....	8
2.1.1.2 Ultrasonic testing .....	8
2.1.2 Types of IRT .....	9
2.1.2.1 Electrical resistance change method paired with IRT.....	10
2.2 Recent advancements in IRT .....	11
2.2.1 Defect depth estimation .....	11

2.3 Recent improvements to CFRP.....	11
2.3.1 Test sample thermal conductivity estimation .....	13
2.4 Applications of JH in composites outside NDE .....	14
2.5 Percolation theory .....	15
 CHAPTER III MATERIALS AND METHODOLOGY .....	 16
3.1 Preliminary materials .....	16
3.2 Preliminary methodology.....	17
3.2.1 Tt.E.C. film adhesive study.....	17
3.2.2 Resin film adhesive preparation.....	18
3.2.3 CFRP coupon preparation.....	20
3.2.4 Sample preparation and bonding .....	22
3.2.5 IRT study setup.....	24
3.3 Investigative materials .....	25
3.3.1 Investigative methodology.....	26
3.3.2 Preliminary bond-line resin QCs .....	30
3.3.3 Investigative bond-line resin QCs.....	33
3.3.4 ZTCFRP-prepreg manufacturing .....	38
3.3.5 OOA-VBO modification.....	42
3.3.6 Defect depth analysis .....	42
3.3.7 Bond-line electrical conductivity consistency study.....	43
3.3.8 Computer aided IRT .....	45
3.3.9 Bond-line uniformity study.....	48
3.3.10 F-IRT setup.....	50
3.3.11 Defect image grading .....	51
 CHAPTER IV RESULTS.....	 55
4.1 Preliminary results .....	55
4.1.1 Film adhesive tray Tt.E.C assessment .....	55
4.1.2 Preliminary thermograms.....	57
4.2 Investigative results .....	59
4.2.1 Investigative thermograms.....	59
4.3 Defect analysis .....	64
4.3.1 Electrical resistivities of bond-line resins with 4-probe measurement .....	64

4.3.2	Defect area similarity parameter .....	65
4.3.3	Defect shape similarity parameter .....	68
4.3.4	Final defect grading .....	70
4.3.5	Defect quality improvement of ZTCFRP over CCFRP .....	71
4.3.6	Direct comparison of JH-IRT and F-IRT methods .....	73
CHAPTER V DISCUSSIONS.....		75
CHAPTER VI CONCLUSIONS .....		79
REFERENCES .....		82
APPENDICES .....		87
Appendix A: Preliminary study .....		87
Appendix B: Investigative study.....		89
B1. Methodology of characterizing the best defect frames using ResearchIR .....		89
B2. Investigative thermal conductivity .....		93
B3. Investigative test sample characteristics .....		94
BIOGRAPHICAL SKETCH .....		97

## LIST OF TABLES

Table	Page
1. NDE methodology for composite damage and defects.....	7
Appendix Tables	
A1. Preliminary IRT results.....	87
A2. Testing sample dimensions and Tt.E.C. for various ACNT, and CNF wt%s.....	88
B1. Physical characteristics of investigative test samples. ....	94
B2. Bond-line characteristics.....	95
B3. JH-IRT thermogram results.....	96



## LIST OF FIGURES

Figure	Page
1. Thermogram of CCFRP and ZTCFRP with copper triangle on heated bed .....	12
2. Two-probe resin resistance evaluation test .....	18
3. Carbon nanofiller film adhesive manufacturing process .....	20
4. OOA-VBO layout .....	21
5. CFRP coupon manufacturing process.....	22
6. CNF 0.8 wt%, 2 wt%, and 4 wt% ready to bond to the CFRP coupons .....	23
7. IRT testing setup.....	25
8. Images show of the outer CFRP surface and bond-line thickness.....	27
9. 4wt% to 1wt% ACNT, conference batch, 100x.....	30
10. 4wt% to 1wt% ACNT, conference batch, 1000x.....	31
11. 4wt% to 2wt% ACNT, conference batch, 100x.....	31
12. 4wt% to 2wt% ACNT, conference batch, 1000x.....	32
13. 4wt% to 3wt% ACNT, conference batch, 100x.....	32
14. 4wt% to 3wt% ACNT, conference batch, 1000x.....	33
15. 4wt% to 2wt% ACNT, 4 hours HSM, remade batch, 100x.....	33
16. 4wt% to 2wt% ACNT, 4 hours HSM, remade batch, 1000x.....	34
17. 3wt% ACNT master batch, 1 hour HSM, remade batch, 100x.....	34

18. 3wt% ACNT master batch, 1 hour HSM, remade batch, 1000x.....	35
19. 3wt% ACNT master batch, 4 hours HSM, remade batch, 100x .....	35
20. 3wt% ACNT master batch, 4 hours HSM, remade batch, 1000x .....	36
21. 3wt% ACNT master batch, 4 hours HSM, 1 hour sonication, remade batch, 100x ....	36
22. 3wt% ACNT master batch, 4 hour HSM, 1 hour sonicated, remade batch, 1000x .....	37
23. Visual representation of an epoxy-CNT mixture undergoing three-roll milling .....	38
24. Prepreg compression plate .....	39
25. Image of 4 plied T700s 1wt% CNF ZTCFRP, 100x .....	41
26. Image of 4 plied T700s 1wt% CNF ZTCFRP, 1000x .....	41
27. Modified OOA-VBO process .....	42
28. Four-probe tool for measuring the electrical resistivity of the bond-line resins.....	44
29. Basic four-probe electrical resistivity tool wiring schematic .....	45
30. Computer aided IRT setup .....	46
31. Improved electrode contacts for JH-IRT .....	48
32. Bond-line consistency test .....	49
33. F-IRT testing setup .....	50
34. Rudimentary defect shape similarity process .....	52
35. Comparison of the preliminary Tt.E.C. measurements.....	56
36. Preliminary Tt.E.C. comparison between CNF and ACNT bonded to CCFRP .....	56
37. The CNF samples taken at the point of clearest image.....	58
38. The ACNT samples taken at the point of clearest image.....	59
39. Control CCFRP 2p: at 30s (JH-IRT) and at 11.60s (F-IRT).....	60
40. 1wt% ACNT CCFRP 2p: at 7.93s (JH-IRT) and at 8.13s (F-IRT).....	60

41. 2wt% ACNT CCFRP 2p: at 10.53s (JH-IRT) and at 11.40s (F-IRT).....	61
42. 3wt% ACNT CCFRP 1p: at 3.33s (JH-IRT) and at 6.07s (F-IRT).....	61
43. 3wt% ACNT CCFRP 2p: at 12.40s (JH-IRT) and at 6.80s (F-IRT).....	61
44. 3wt% ACNT CCFRP 4p: at 28.00s (JH-IRT) and at 18.47s (F-IRT).....	62
45. Control ACNT ZTCFRP, 2p at 30s, both cases.....	62
46. 1wt% ACNT ZTCFRP 2p: at 9.8s (JH-IRT) and at 13.9s (F-IRT) .....	62
47. 2wt% ACNT ZTCFRP 2p: at 12.93s (JH-IRT) and at 9.13s (F-IRT) .....	63
48. 3wt% ACNT ZTCFRP 1p: at 7.93s (JH-IRT) and at 5.87s (F-IRT). .....	63
49. 3wt% ACNT ZTCFRP 2p: at 5.33s (JH-IRT) and at 8.87s (F-IRT). .....	63
50. 3wt% ACNT ZTCFRP 4p: at 8.13s (JH-IRT) and at 59.33s (F-IRT). .....	64
51. 4 probe bond-line resistivity results.....	65
52. Defect area similarity for samples of two plied ZTCFRP and CCFRP (JH-IRT) .....	66
53. Defect area similarity for ZTCFRP and CCFRP of various ply thicknesses (JH-IRT).....	67
54. Shape similarity of ZTCFRP and CCFRP bonded to various wt% ACNT (JH-IRT).....	68
55. Shape similarity of ZTCFRP and CCFRP of various ply thicknesses (JH-IRT).....	69
56. Average grading of ZTFRP and CCFRP with various wt% ACNT (JH-IRT) .....	70
57. Average grading of ZTFRP and CCFRP with various ply thicknesses (JH-IRT) .....	70
58. Improvement of ZTCFRP over CCFRP with various wt% ACNT (JH-IRT) .....	71
59. Improvement of ZTCFRP over CCFRP with various ply thicknesses (JH-IRT) .....	72
60. Comparing useful defect time for IRT cases of various ACNT wt% s .....	74
61. Comparing useful defect time for both IRT cases with various ply thicknesses .....	74

Appendices Figures

B1. ResearchIR user interface.....90

B2. Offset and fixed temperature range implementation.....91

B3. BF for test sample 3wt% ACNT ZTCFRP 1ply, (JH-IRT).....91

B4. Placing the grid overlay onto the thermogram.....92

B5. The resulting defect area and shape similarity estimation .....92

B6. Thermal conductivity estimates for CCFRP and ZTCFRP coupons used for this study  
(Left to Right, respectively).....93

## LIST OF ABBREVIATIONS

3D	Three-dimensional
ABS	Acrylonitrile butadiene styrene
ACNT	Arkema CNT
CCFRP	Control carbon fiber reinforced polymer
CF	Carbon fiber
CFRP	Carbon fiber reinforced polymer
CNF	Carbon nanofiber
CNT	Carbon nanotube
COV	Coefficient of variance
DC	Direct current
F-IRT	Flash thermography
ILSS	Interlaminar shear strength
JH	Joule heating
JH-IRT	Joule heat infrared thermography
NDE	Non-destructive evaluation
Tt.E.C.	Through-thickness electrical conductivity
Tt.T.C.	Through-thickness thermal conductivity
ZTCFRP	Z-Threaded carbon fiber reinforced polymer

## ABSTRACT

William W. Taylor, M. S., University of South Alabama, June 2023. Examining the Efficacy of using IRT as an NDE method for CFRP and ZTCFRP Composites. Chair of Committee: Kuang-Ting, Hsiao, Ph.D.

A film adhesive is commonly used to form the bond-line between composite parts. The bond-line's quality and performance can be affected by defects such as voids, impurities, and agglomerations. Identifying these defects is possible with non-destructive evaluation testing (NDE). In this thesis, the joule-heating effect (JH) through carbon nanofiber (CNF) and carbon nanotube (CNT) modified film adhesive bonded to control carbon fiber reinforced polymer (CCFRP) was used along with infrared thermography testing (IRT) for bond-line defect inspection as a preliminary study. Due to the difference in the electrical conductivity between the modified epoxy and the defect, JH can cause a difference in temperature that can be viewed by IRT. The percentage of carbon nanofiller in a film adhesive is related to its electrical conductivity. A three-dimensional (3D) printed acrylonitrile butadiene (ABS) equilateral triangle defect was used. A more in-depth investigation was conducted to determine how both the number of plies and z-threaded carbon fiber reinforced polymer (ZTCFRP) can influence the defect image. Flash thermography (F-IRT) was used to provide a comparison against this NDE method.

## **CHAPTER I**

### **INTRODUCTION**

Carbon fiber reinforced polymers (CFRPs) are a group of composite materials which have a high strength to weight ratio compared to metals as well as the versatility to find use in many industries because of their ability to be a multi-functional material. A multi-functional material has the ability to adapt to many different industries to fit requirements not currently met, such as those involving cost, time, or any other factors which make any other material a liability. CFRP can do this through changing the types of resins and carbon fiber (CF) used in its manufacturing. Manufacturing industries like the automotive, sports, aerospace (both commercial and spacefaring), energy storage, repair, computer protection, and polymer-based circuitry can and have benefited from this material in some way or another [1]. In terms of finance, a study found that the CF global demand across material intensive industries such as the construction, automotive, renewable energy (wind), and aerospace industry will have a compound annual growth rate of 10.9% from 2017 to 2025. In other words, the CF industry in 2017 was worth \$2.25 billion which is projected to rise to \$5.15 billion in 2025 [2].

This projected global growth will depend on a solid sense of reliability in the material for it to be fully realized. Evaluation of structural materials is of paramount importance to any industry in which the safety and reliability of the material can be

trusted in many engineering designs. While many kinds of damage to the structure can give insight into the likelihood of failure, the damages to the interior are more complicated to examine. There are two kinds of common evaluation tests, non-destructive and destructive, and both can characterize the nature of damage to a part although they differ in an important way. Non-destructive evaluation testing (NDE) will leave the part being analyzed without any structural liability while destructive evaluation testing will. This difference can carry implications for cost, labor, and the overall health of a material the customer will face. Because of this, the use of NDE is clearly preferred. Due to the nature of the samples used in this study, it was impossible to inspect for internal damage physically within the samples without destroying them in the process. This reduced the accuracy and repeatability of quality test samples. This thesis aims to characterize internal defects of a bond-line between two CFRP parts with the use of a novel NDE method.

### **1.1 Thesis hypotheses**

This thesis is composed of two studies in which one acts as a preliminary study and the other as an investigative study. The preliminary study focuses on whether CNF or ACNT enriched resin bond-lines would be better suited to provide a clearer defect image in a composite lap joint being examined with joule heated IRT (JH-IRT). The investigative study focuses on whether CCFRP or ZTCFRP would provide a clearer image of the defect within the bond-line following a similar procedure used in the preliminary study.



### **1.1.1 Preliminary feasibility hypothesis**

The electrical and thermal conductivity of CNF and ACNT bond-lines could be used as a medium in which IRT NDE could detect and characterize the internal defects within a CFRP lap joint. The CF itself is vastly more conductive as opposed to the epoxy which binds it together. JH is the phenomenon in which electrical current passing through an object with internal resistivities releases energy through the form of heat. If the epoxy layering on the outside of a CFRP lap joint was to be removed through sanding and polishing the CFRP fiber matrix would be exposed. If this was then subjected to a direct current from one end of the CFRP to the other, it should release heat at the point of lowest resistivity.

In this case, a CFRP test sample connected to a conductive epoxy bond-line should produce a temperature signature at the bond-line if current flows through the two sides of CFRP. While heating in the CFRP would be present, the resistance of the fiber-epoxy matrix compared to the epoxy matrix at the bond-line would be very small. Note that the CNF/CNT modified bond line can also increase the mechanical strength of the bond-line [3, 4]; hence, the CNF/CNT modified bond-line can have multifunctional purposes as well. A composite with a higher through-thickness electrical conductivity (Tt.E.C.) could be used to create a lightweight, yet very conductive, composite to combat lightning strike damage on the exterior of an aircraft [5].

Now if a manufactured defect was placed into the bond-line and was subjected to direct current, the defect would affect the temperature signature at the bond-line. The defect, in this case made of ABS, has a different thermal and electrical conductivity than

the surrounding bond-line. The defect's outline and general presence would be detected by an infrared camera as direct current passes through the CFRP lap joint.

For this case, a few assumptions must be made:

1. The CFRP coupons have little to no voids.
2. The overall electrical and thermal resistivity of each test sample's coupon are consistent with their CCFRP or ZTCFRP case, respectively.

### **1.1.2 Improved investigational hypothesis**

As the preliminary hypothesis provides a basic outlook for this novel NDE method, a more in-depth and robust understanding is required for further research insights. Continuing beyond the preliminary methodology, some techniques to make the defect within the bond-line easier to detect and characterize include:

1. Increasing the thickness of the defect; more energy would be needed to make the temperature of the defect reach the temperature of its surrounding bond-line.
2. Increasing the applied power output; a higher wattage would mean more heat imposed onto the bond-line which could produce a JH-IRT defect image more quickly. The increased wattage should also increase the contrast between the defect and its surroundings, allowing a sharper defect profile. Additionally, this increased heat flux could saturate the image and possibly reduce the useful time in which the defect can be observed. This means the defect area could reach the surrounding bond-line temperature faster.
3. Increasing the electrical conductivity of the bond-line; increasing the amount of ACNT within the bond-line would allow for more connections of ACNT within the resin matrix nanostructures to form before diminishing returns dampen the

clarity from the added ACNT due to the percolation limit. This is not unlike Velcro, where increasing the number of hooks and burrs provides more adhesion to each other.

4. Increasing the electrical conductivity of the CFRP coupons; by making ZTCFRP coupons with CNF aligned in the through-thickness direction, the electrical conductivity would surpass the performance of the original study's control CFRP coupons. This should increase the quality of the defect images as well.

The takeaway from these hypothetical pros and cons would be for the implementation of ZTCFRP to replace the control CFRP coupons from the original study to produce higher quality defect images through JH-IRT.

## **1.2 Thesis objectives**

A list of thesis objectives are as follows:

1. Create various bond-line films at different wt% of ACNT of consistent thickness for both the preliminary and investigative studies.
2. Characterize how ply depth influences the defect image for CCFRP and ZTCFRP test samples in the investigative study.
3. Detect and characterize the bond-line defects based on visual quality for both studies.
4. Determine the difference between test samples bonded with CCFRP over ZTCFRP's defect images.

5. Determine the effectiveness of this novel NDE method against another NDE method, flash thermography (F-IRT).
6. Quantify grading the defect image based on the amount of defect area detected as well as the likeness in shape of the defect.

**CHAPTER II**  
**LITERATURE REVIEW**

**2.1 NDE summary**

There are many NDE methods for composite materials that can characterize different forms of structural damage within. A summary regarding these methods and the applicability of detecting these damages is listed below [6].

Table 1: NDE methodology for composite damage and defects [6].

Composite Part	Defect	Thermography	Pulse/Echo	Acoustic Emission	X-Ray
Bond-line	Debonding	☑	☑	☑	☑
	Voids	☑	☑	☑	☑
	Cracks	☑	☑	☑	3
	Porosity	☑	☒	☒	☑
	Moisture	☒	☒	☒	☑
	Lack of adhesive	☒	☑	☑	☑
Laminate	Delamination	☑	☑	☑	3
	Fiber breakage	2, 3	☒	☒	☑
	Heat damage	☒	☒	☒	☒
	Voids	☑	☑	☒	☑
	Macrocracking	☑	☒	☑	3
	Ununiform cure	2	☒	☒	☒

1 = Open to surface, 2 = Unreliable, 3 = orientation dependent

### **2.1.1 Contact NDE methods**

Contact NDE involves direct contact of the measurement device onto the part being examined. This often involves specialized equipment and significant time investment and is good for small scale examinations.

#### **2.1.1.1 Electrical impedance tomography.**

This NDE method employs electrodes placed onto a CFRP panel then imposes DC current into the part. As current passes through, small changes in the output voltage measurements occur due to the part's interior not being fully homogenous in its resistivity distribution. Taking these measurements into account, a map of the panel is created and signifies how 'healthy' the part is in regard to structural defects. When damage is imposed, whether it be from wear and tear throughout its useful life or a manufactured internal defect, the resistivity distribution is altered and warps the map around the damaged area. This approach depends most heavily on the resistivity of the composite for a clear image of the damage to be seen, CFRP being an excellent example [7]. This concept was further researched to characterize damage detection for unidirectional CFRP. A limiting factor for the usefulness of this NDE method is the reliance of electrically conductive composites. A study was conducted to gauge the accuracy of damage detection for a unidirectional CFRP composite and was successful by carefully spacing off electrodes and reading the resistances between them [8].

#### **2.1.1.2 Ultrasonic testing.**

As the name suggests, this method of NDE utilizes ultrasound to determine the damage inside a material or part. This is accomplished through sound wave excitation from a special probe of a piezoelectric material which emits sound waves at a specific

frequency. This signal permeates through the material more effectively with the addition of a coupling agent to provide a tight seal around the probe and surface of the part.

Defects are detected as the sound wave reflects away from the defect cavity and back to the probe. The excitation and response of sound waves are converted into a signal which can be displayed through a screen. As the probe moves across a defect, the usual signal is disrupted since one surface is closer to the front of the material than the back side of it [9].

### **2.1.2 Types of IRT**

IRT is a non-contact NDE method which determines the temperature response of a material under a heat flux which can be interpreted as a defect within using an infrared camera. IRT can come in the form of passive or active implementation. IRT relies on the examined materials' intrinsic thermal and electrical properties. In a composite, some materials which are bonded together might have dissimilar electrical and thermal properties. When dealing with CFRP, the outer and inner epoxy layers function as both an insulator and resistor whereas the CF layers conduct heat and electricity. This difference in conductivity allows areas of the composite to warm at a different rate which allows the infrared camera to characterize it. In IRT, this difference can be due to a void, delamination, or other interfacial defects. The defect displayed would have a distinct heat signature when an external heating source radiates heat onto the exterior or interior of the part being evaluated. This method is useful for detecting defects across a large area and is done without contacting the part making it easier to implement [10]. The reflected temperature signature coming into the infrared camera allows a view of structural defects such as voids, agglomerations, and delamination of ply-layers within composites. This is

due to the differences in electrical and thermal conductivity between the defect and the composite part [11].

#### **2.1.2.1 Electrical resistance change method paired with IRT.**

As stated in section 1.1.1, JH-IRT is the output heat from electrical current passing through a resistive medium. This conversion can be summarized in the equations below.

$$P = I^2 R \quad (1)$$

Electrical power (P) is measured in watts (w) and is determined by the product of current (I) squared and the resistance (R) of the material being imposed with current. If a material has a uniform electrical conductivity as well as a uniform electrical resistance, the resulting heat flux across the material would be homogenous. However, differences in these parameters are probable. These differences influence the output power and heat flux and cause non-uniformities in the temperature profile of the material. The less the resistance, the greater the JH. One study found that damaged CFRP, surface indentation, could be examined for interior cracking with the use of electrodes imposing a direct current onto the part. When imposed with current in the through-thickness direction, the current flowed through the path of least resistance and ‘coalesced’ in areas that had experienced trauma. This current concentration heats the damaged surface and sub-layer damage more than the surrounding CFRP. This was caused by the indentation damage and resulted in the thinner CFRP layers having a reduced electrical resistivity which in turn allowed more JH to take place [12].



## **2.2 Recent advancements in IRT**

### **2.2.1 Defect depth estimation**

Beyond the apparent usefulness of IRT to show damage to a composite under its surface, the subtle, yet important, image data can disclose a much more detailed account of the damage than the original image can provide. IRT excels in testing large areas for defects and damage while also doing it quickly compared to other NDE methods. IRT also has a wider scope of materials it can analyze. This multi-material damage analysis is extremely effective when examining composites [13].

### **2.3 Recent improvements to CFRP**

Epoxy-based resin has a low electrical conductivity with an average E.C. of  $2.3 \times 10^{-8}$  S/m [14]. This low E.C. does a disservice to the highly conductive CFs within a Tt.E.C. range of  $10^{-3} - 10^0$  S/m [15.]. By incorporating carbon nanofillers into the resin matrix, the Tt.E.C increases. Some carbon nanofillers such as CNTs can have an average range of E.C. of  $10^4 - 10^7$  S/m [16] or CNF with an average E.C. nearly  $10^5$  S/m [17].

In relation to NDE, CFRP and the bonds between them can be analyzed and can detect structural defects hidden within. Because of this, a kind of material which both possesses high thermal and electrical conductivity whilst remaining structurally sound is desired. ZTCFRP is a strong candidate to meet these demands. The multi-functional material is infused with CNFs which are aligned in the through-thickness direction

through the composite. This acts to enhance the composites' interlaminar shear strength (ILSS), Tt.E.C., and Tt.T.C..

In recent years, understanding the mechanical, material, thermal, and electrical properties of ZTCFRP have opened many avenues for both aerospace and defense applications. Note that unidirectional ZTCFRP laminates compared with the traditional CFRP laminate's Tt.E.C were found as 16.24 S/m vs 0.161 S/m, respectively (a 9,987% enhancement) [18]. In addition, the ZTCFRP laminate has significantly higher Tt.T.C. (Tt.T.C.) of 9.85 W/m-K compared with traditional CFRP's 1.31 W/m-K (approximately 7.5 times higher). Another benefit of using z-aligned film to bond ZTCFRP laminates could be in reducing the apparent stretching of the defect image due to the unidirectional CF [19].

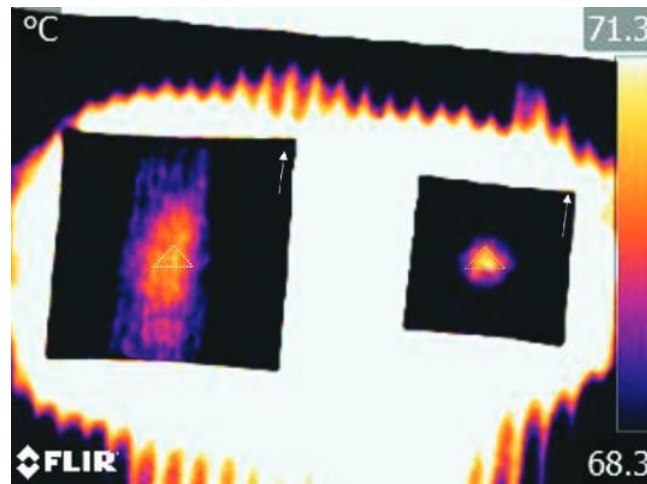


Figure 1: Thermogram of CCFRP and ZTCFRP with copper triangle on heated bed. The white arrow signifies the fiber direction of the unidirectional AS4 CF.

[Permission to use image from reference [19] granted].

### 2.3.1 Test sample thermal conductivity estimation

The Tt.T.C. of the test samples is as important as the electrical conductivity of the bond-line. The Tt.T.C. determines how much heat is transferred from the bond-line JH. Techniques for accurately estimating the Tt.E.C. of CCFRP and ZTCFRP were investigated by characterizing the nanostructure of these composites using a series of logic models. The following equations were used to estimate the volume of CNF, the volume of resin within the composite, and the estimated thermal conductivity of CCFRP and ZTCFRP [19].

$$V_{CNF} = (1 - V_{CF}) \frac{\frac{w_{CNF}}{\rho_{CNF}}}{\left(\frac{w_{CNF}}{\rho_{CNF}}\right) + \left(\frac{w_R}{\rho_R}\right)} \quad (2)$$

$$V_R = 1 - V_{CF} - V_{CNF} \quad (3)$$

$$K_{e,CCFRP} = \frac{1}{\left(\frac{V_{CF}}{K_{CF}}\right) + \left(\frac{V_R}{K_R}\right) + \left(\frac{V_{CNF}}{K_{CNF}}\right)} \quad (4)$$

$$K_{e,ZTCFRP} = \frac{1}{((V_{CF})/K_{CF}) + ((V_R + V_{CNF})^2 / (K_R V_R + K_{CNF} V_{CNF}))} \quad (5)$$

The thermal conductivity equations were compared to known values in the manufactured composites to find the relative error. The relative error taken from these comparisons were 58% and 116% for CCFRP and ZTCFRP, respectively. These relations were used to estimate the thermal conductivities of the composites used in this study which aided in determining trends found in data later. While the CF used in that study and this thesis are different, AS4 and T700S, the mechanics of how CNF interacts within the fiber epoxy matrix are similar, if not identical.

## **2.4 Applications of JH in composites outside NDE**

The use of JH in this context is not constrained to NDE. JH has various applications to harness heat safely through careful design and implementation. One application utilizing this phenomenon was found by mixing CNT into cement used in an electrically heated asphalt system to enhance its heating efficiency [20], This implementation offset the need for labor and chemical means such as rock salt to melt ice which could impact the salinity of ground soil and corrosion rates in the immediate vicinity. The researchers found that pairing 1wt% CNT and 1wt% CF inside a cementitious composite would decrease the electrical resistivity and generate significantly more heat than other arrangements of CNT and CF in the study. The maximum temperature from this best performing arrangement was 70°C after 10 minutes of constant voltage of 8v. However, the addition of CNT for this system was found to be misplaced as the cracks that generate inside the cement when exposed to the elements would sever electrical connections within the cement and reduce its effectiveness in heating. Researchers have used JH to aid in making CFRP by directly imposing electrical current onto the CFs which were impregnated with resin beforehand. Complex composite geometries in three-dimensions can also be cured via JH which can provide many applications into the automotive and aerospace industries [21]. However, the electrical resistance of the CFRP depends on the arrangement of the lamina. JH has also been reported for curing epoxy composite adhesives paired with strong electrical conductors such as bucky-paper (very thin sheets made of multi-walled CNTs) and achieved a 67% improvement in bonding strength over cured pure epoxy [22].

## **2.5 Percolation theory**

Another way to promote more heat to pass through a composite part would be to increase thermal or electrical conductivity by implementing conductive materials into the composite's manufacturing process. However, there are limits to how much a material can become conductive before facing diminished returns or worsening of apparent conductivity. Percolation theory describes electrical conductivity compared against the weight percentage of the conductive material within the composite. While it is true this would increase with the amount of CNF added, it is not a linear relationship but instead resembles a power rule function. When adding more CNF into the epoxy matrix the electrical conductivity would rise sharply yet taper off and remain at a consistent value regardless of how much is added to it [23]. In an unaligned CNF CFRP, many of the nanofillers would act similarly to wires as more connect through the CFRP panels. Although the orientation of the nanofiller is not controlled in this case, the risk of the nanofiller clumping together from surface tension and electrical charge would be higher and can result in interior defects as well as a reduction in the electrical conductivity.

## **CHAPTER III**

### **MATERIALS AND METHODOLOGY**

#### **3.1 Preliminary materials**

The materials used in this experiment include PR-24-XT-HHT grade CNF (Pyrograph Products/Applied Sciences, Inc.), Graphistrength CS1-25 CNT (Arkema Group), T700s unidirectional CF fabric (680 g/m<sup>2</sup> areal weight, 12k tow size, and 1.8 g/cm<sup>3</sup> fiber density, Toray), Epikure-W curing agent and Epon 862 epoxy resin (mixing ratio 26.5:100) (Miller-Stephenson Chemical Co. Inc.), surfactants S-191 and S-192 (BYK), 120 grit, 320, 400 grit, wet 800 grit 3M sandpapers, half-hard 110 copper sheet metal, and Hillman 6063-T5 aluminum sheet metal.

Optical hardware includes a Flir E40 thermal infrared camera, a Nikon Eclipse LV150 microscope for sample quality analysis. A 210W GW Instek PSP-603 power supply as well as an Agilent 34405A  $5\frac{1}{2}$  digit multimeter. A dual channel Danoplus high accuracy digital k-type thermocouple (Amazon) was used to calibrate the thermal infrared camera.

## **3.2 Preliminary methodology**

### **3.2.1 Tt.E.C. film adhesive study**

Resins infused with varying amounts of conductive nanofillers were investigated to understand the percolation trends of CNF and ACNT. The minimum concentration used was 1 wt% nanofillers for this test and 0.8 wt% for the bond-line tests. This was due to a ratio mistake. The resistance and geometry of the resin sample must be known to estimate the Tt.E.C.

In order to do this, the geometry of the ACNT enriched resin was constrained by creating a 3D printed housing for the resin's electrical resistance to be measured (Figure 2). ABS was chosen as it had a glass transition temperature of approximately 105 °C [24] and does not melt until reaching at least 200 °C [25]. This meant it could hold a sample of resin and then directly cure at 120 °C for two hours without deforming significantly for later measurement. A copper sheet was cut into approximately one square inch pieces and sanded with 220 grit sandpaper. This was then fitted into the tool listed in Figure 2. The Epon 862 epoxy resin, infused with various weights of ACNT and mixed with an appropriate amount of Epikure-W curing agent, was poured into the bottom copper sheet, and covered with the top copper sheet. The bottom and top ABS trays had small holes exposing the back side of the copper sheets which allowed the multimeter's probes to read the resistance of the resin sample sandwiched between the two electrodes. The sample was cured in a vacuum oven for two hours until cured (120 °C). After being allowed to cool for five minutes at room temperature (22 °C), the electrical resistance was measured using the multimeter. By this assessment, 1 wt%, 2 wt%, 3 wt%, and 4 wt%

ACNT and CNF at the same concentrations were chosen to be the bond-line nanofillers for the thermographic NDE defect testing based on the electrical conductivity measured.

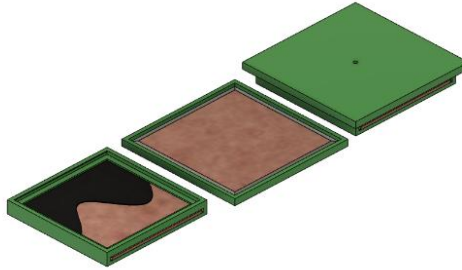


Figure 2: Two-probe resin resistance evaluation test. The test is comprised of the bottom resin tray, top resin tray, and the completed assembly (left to right).

The electrical resistance ( $R$ ), the bond-line area ( $A$ ), and thickness of the bond ( $t$ ) of the sample were recorded. The electrical conductivity of the material was calculated using the following mathematical relationship:

$$\sigma = \frac{t}{R A} \quad (6)$$

### 3.2.2 Resin film adhesive preparation

In order to create the film adhesives used in testing, only one main process was needed for both CNF and ACNT. The only difference in preparing these nanofillers into film adhesive was that the ACNT was submerged in a rationed amount of Epon 862 overnight in a vacuum oven at 90 °C. The ACNT came in the form of pellets at room



temperature, which already had its CNT (about 25wt% concentration) well dispersed in the solid bisphenol-A epoxy. As shown in Figure 3, both ACNT and CNF based film adhesives followed the rest of the process once the first round of high shear mixing (HSM) occurred. The manufacturing of CNF-based film adhesives started by measuring out one-part Epon 862 and 0.265 parts of Epikure-W by weight. Then the surfactants S191 and S192 were rationed to the same weight fraction of CNF (i.e., 4.0wt%). The CNF-Epon 862 batch was manually mixed to minimize CNF clumps. After the mixture appeared approximately homogeneous, it was placed onto a hotplate at 90 °C and high shear mixed (HSM) with an industrial stirring machine for one hour at 300 rpm. The direction of rotation was switched at 30 mins for even mixing. Then, a sample was taken for quality assessment using the Nikon Eclipse LV150 microscope. The quality of the batch was checked after sonication concluded, and if the dispersion of CNF seemed adequate, the batch would undergo dilution. Portions of the 4 wt% CNF batch were set aside and mixed with a rationed amount of Epon 862 to create 0.8 wt%, 2 wt%, and 3 wt% batches. The dilution process was performed the same for both nanofillers. Finally, thirty grams of each batch were poured into a proper amount of Epikure-W and hand mixed to complete the resin blends. After mixing, the beakers were put through the B-stage process and had their temperature and their cure cycle monitored. The B-staging operation finished at about 35-40 min at 120°C. Once the batches reached B-stage, they were poured onto a sheet of parchment paper on a hotplate of about 60-70°C. The parchment paper was put under a metal sheet raised off the

hot plate with metal shims to create an approximately consistent film thickness (0.30-0.60 mm). Finally, after passing through the gap, the CNF film adhesive was created.

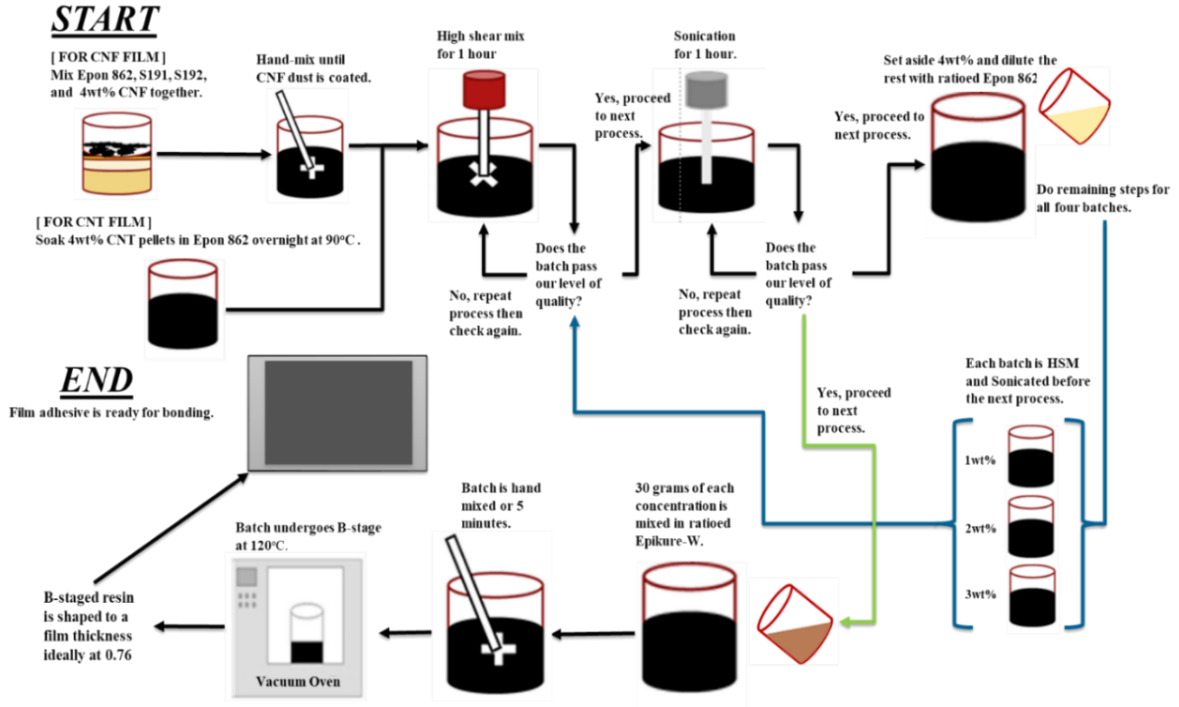


Figure 3: Carbon nanofiller film adhesive manufacturing process.

### 3.2.3 CFRP coupon preparation

The type of CF is an important distinction to make for this study. Material properties such as permeability, fiber porosity, areal weight, density, fiber loading arrangement, and the sizing of the strands of CF will affect the composite in both manufacturing and testing aspects. For this study, three CF fabrics, AS4, AS7, and T700S were considered for testing. T700S was chosen due to the thickness of each lamina reaching the desired prepreg thickness.

T700S unidirectional CF fabric was cut into an 18 x 6-inch rectangle with the unidirectional fiber parallel to the 6-inch length. thirty grams of control epoxy resin was

created by mixing one-part Epon 862 to 0.265 parts Epikure-W curing agent, then hand mixed for five minutes, alternating directions occasionally. The resin was then impregnated into the CF fabric using a resin roller. The resin impregnated fabric was placed onto an industrial hot press for 25-30 min at 120 °C. to reach B-stage and form the prepreg. The prepreg was taken from the oven and allowed to cool for fifteen minutes at room temperature.

The prepreg was cut into six pieces and placed on the Out of Autoclave Vacuum Bag Only (OOA-VBO) setup (Figure 4) to be further cured into six single layer CFRP panels. The prepreg was first vacuumed to -86 KPa and then was placed into the hot press for two hours to cure and then demolded (Figure 4). After the OOA-VBO process, the single layer CFRP coupons were sanded down on both sides with 120, 320, 400, and wet 800 grit sandpaper until the surfaces were smooth to the touch. This threshold of smoothness was reached at approximately 0.60 mm thickness, starting from the CFRP thickness of approximately 0.65-0.7 mm. After the sanding process, the coupons were placed in a soap-water bath to remove dust from sanding and then dried in an oven for five minutes. They were then left to cool at room temperature for another five minutes. A light wash of acetone on the coupons was applied and completed the CFRP coupon preparation.

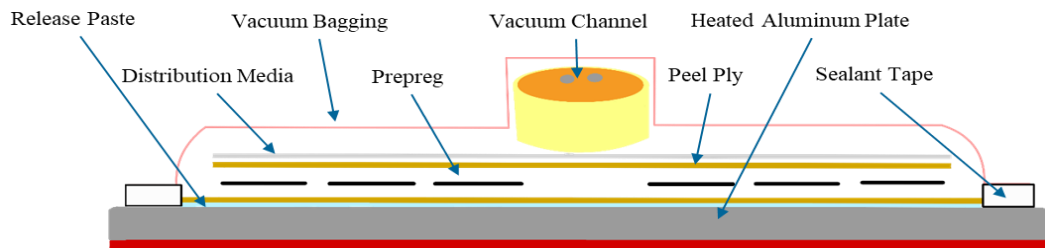


Figure 4: OOA-VBO layout.

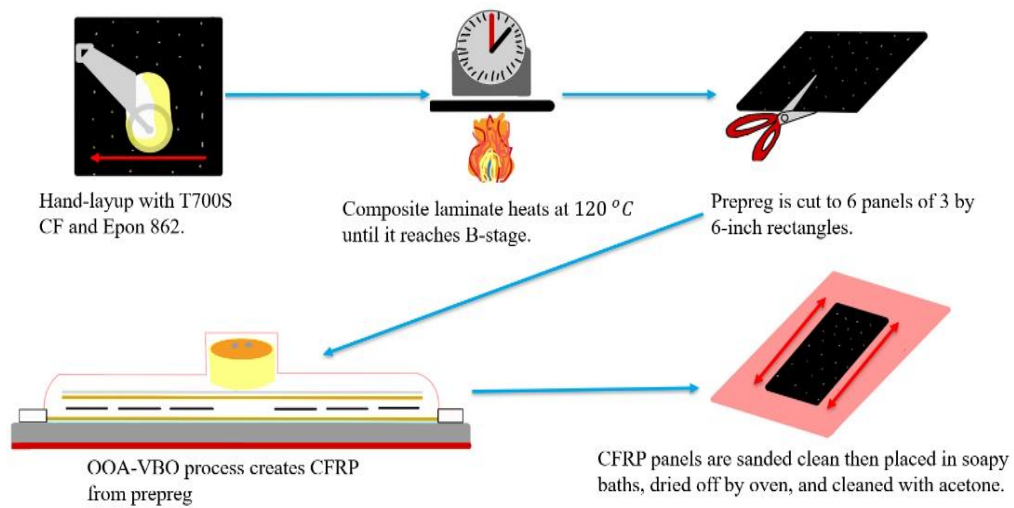


Figure 5: CFRP coupon manufacturing process.

### 3.2.4 Sample preparation and bonding

The film adhesive and the CFRP panels were brought together to create the testing sample (Figure 5). This was started by measuring a 76.2 mm x 76.2 mm (3 x 3-inch) square onto the film adhesive's parchment paper layer then cutting out the square shape film adhesive. A 3D printed ABS triangle punch card was used to make an indentation of a triangle with 30 mm sides. If a film adhesive was too sticky due to insufficient B-stage treatment, it would be placed into the freezer for at least 10 seconds to become rigid to the touch. If the film adhesive was too thin to meet the height of the ABS defect (0.76mm after sanding with 400 grit sandpaper) an additional layer of film adhesive would be added on top. The indentation was scrapped off carefully using a thumbtack to leave a triangular void with a clean CFRP surface surrounded by the film adhesive. Once completed, the ABS triangle defects were inserted. The back of the CFRP coupon was marked where the defect was on the other side. The top CFRP panel was rolled and pressed carefully from side to side to limit the amount of air trapped inside while bonding. Then, the testing

samples were put into a vacuum oven for two hours. Once the curing process concluded, the edges and sides of the test samples were sanded and polished following the same cleansing process as for cleaning the CFRP coupons. By doing this, the voltage applied, ideally, will only create current cross through the bond-line in the thickness direction rather than finding any other bypath. Prior to testing, the ends of the CFRP samples were sanded gently with 220 grit sandpaper to remove any epoxy coating and cleaned with acetone to reduce any surface contact resistance. The bonding setup is shown in Figure 6.

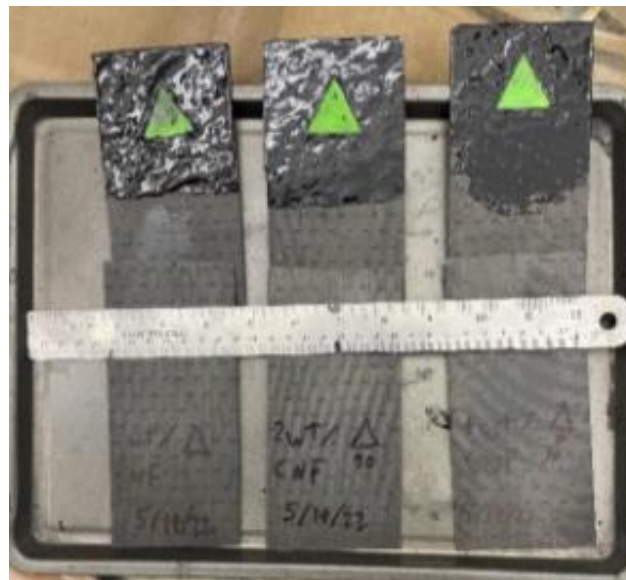


Figure 6: CNF 0.8 wt%, 2 wt%, and 4 wt% ready to bond to the CFRP coupons.

In this experimental study, to ensure the most current permeates through the bonded CFRP testing samples, highly electrically conductive metals, aluminum, and copper were used as electrodes to connect to the single-lap bonded CFRP samples. Aluminum and copper have an electrical conductivity of  $3.5 \times 10^7$  S/m and  $5.3 \times 10^7$  S/m, respectively [26].

### 3.2.5 IRT study setup

The defects within the CFRP film adhesive bond-line were evaluated with a thermal infrared camera. The camera was mounted 12 inches away from the testing sample to allow a full view of the bonding area. Calibrating the infrared camera (including the emissivity input) was achieved through monitoring the temperature it was measuring as compared to a thermocouple in the same region underneath the sample. Different regions and hot spots on the bond area were measured this way as well to gauge the accuracy of the camera. This calibration practice was inspired by researchers who determined the emissivity of aluminum AW 6082 for their infrared camera [27]. Vice grips that held the testing sample in place were modified by adding an ABS printed arch to allow some pliers to press firmly onto the aluminum strips (as electrodes) onto the exposed CFs of the CFRP panels. The cables from the power supply were connected onto the two strips of acetone cleaned aluminum sheet metal of approximately 25.4 mm x 76.2 mm (1 by 3 inches) area with a thickness of 0.77 mm. As the ABS defect was nonconductive, the electrical current could not pass through it. Instead, the electrical current went through the bond-line which invoked JH. From this difference in electrical conductivity, the defect should be shown as a colder region compared with the rest of bonded area and can be recorded with the infrared camera. This bond-line IRT NDE experimental setting is shown in Figure 7.

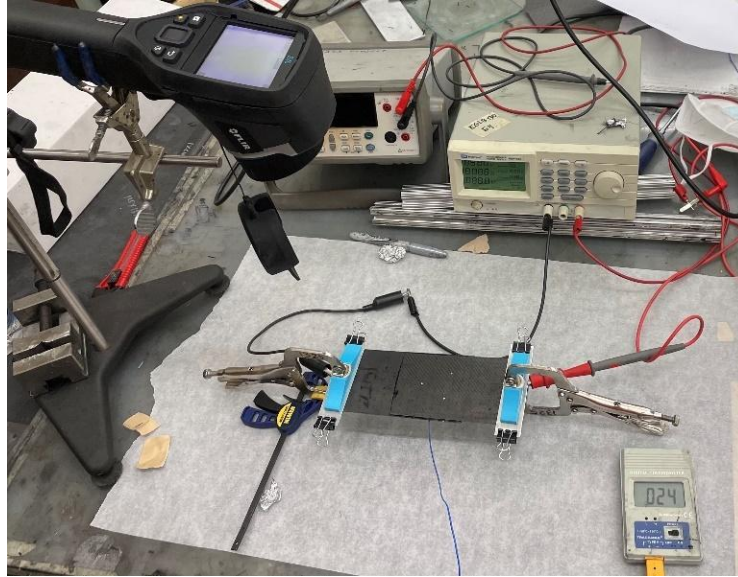


Figure 7: IRT testing setup.

As shown in Figure 6, the camera pointed directly onto the center of the triangle spot indicated by the markings given before bonding. The infrared camera's emissivity preset for carbon ( $\epsilon = 0.95$ ) was used due to the dark and low reflectivity of the CFRP testing sample, which gave the closest measurements with the thermocouple that measured between 1 – 2°C cooler.

### **3.3 Investigative materials**

As this next aspect of research is a direct follow-up to the preliminary study, several of the materials from that are reused with a few exceptions. The materials include PR-24-XT-HHT grade CNF (Pyrograph Products/Applied Sciences, Inc.). Graphistrength CS1-25 CNT (Arkema Group). T700S unidirectional CF fabric (680 g/m<sup>2</sup> areal weight, 12k tow size, and 1.8 g/cm<sup>3</sup> fiber density, Toray). Epikure-W curing agent and Epon 862 epoxy resin (mixing ratio 26.5:100) (Miller-Stephenson Chemical Co. Inc.). Surfactants S-191

and S-192 (BYK). 3M sandpaper of grit sizes 80, 120, 320, 400, wet 800, wet 1500, and wet 3000. Half-hard 110 copper sheet metal and Hillman 6063-T5 aluminum sheet metal. Airweave N-10 breather fabric and Wrightlon 5200B release film (Airtech) were used during the out of autoclave vacuum bag only (OOAVBO) process to cure the composites.

### **3.3.1 Investigative methodology**

With hindsight from the resulting preliminary work, ways to understand and enhance the visual quality of the defect infrared image were conducted. After the preliminary study, some aspects of the bond-line quality were less than desired. The uneven thickness and the resin leakage onto the CFRP coupons lessened the effectiveness for heat to transfer from the top coupon through the bond-line and then through the bottom coupon. The unevenness allowed ‘hotspots’ on the bond-line area as parts which were closer together and allowed a shorter distance for the heat to diffuse. This caused issues in analyzing the infrared thermographic defect images where the hotspots outshined the subtle temperature difference the defect would have had with its surroundings. In order to combat this issue, a new technique for bonding was needed.

A simple, yet effective, change was wrapping the entire test sample outside the bonding area with layers of Kapton tape. After the bond-line cured after two hours inside a 120°C vacuum oven at one atmosphere of pressure, Kapton tape was peeled away from the sample which removed any resin leakage that could have cured onto the CCFRP or ZTCFRP coupons. This produced higher quality samples than those from the preliminary study.



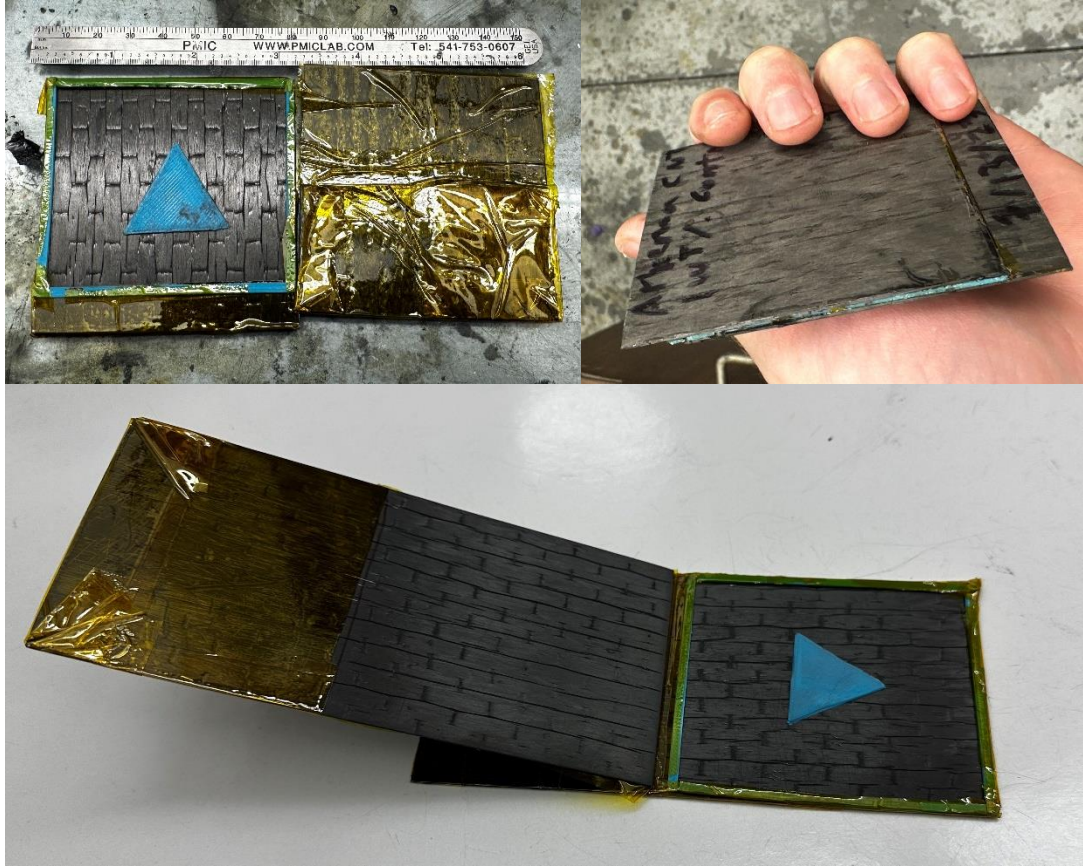


Figure 8: Images show the outer CFRP surface and bond-line thickness. The two test coupons were attached with a latch attachment (below).

Another concern was the presence of air pockets inside the cured bond-lines which would affect the transfer of heat through the bond as well as obscure the defect area. In the previous study, a B-staged film adhesive was passed through a carefully leveled gap to achieve the desired film thickness. The resulting film adhesive was overlaid onto the coupon's bonding area and placed into a freezer at  $-17^{\circ}\text{C}$  until the film was rigid. When this occurred, a portion near the center was removed by scratching a thumb tack across the film's surface to put the defect in its place.

This process of implanting the defect was labor intensive and was replaced by pouring the liquid resin into the bond-line area surrounded with dams and then placing the defect inside. Care was given to laying the defect as well as the top coupon over the bond-line to limit the chance of air becoming trapped while it cured. The samples were ‘practice’ bonded with Kapton tape to ensure everything was tightly sealed. One coupon was then attached beside the bond-line to restrict any movement other than the direction to seal the bond. Placing the parts side to side was the chosen approach.

Finally, the test sample was placed onto an industrial heating press pre-heated to 120°C and covered with parchment paper to reduce the cleaning time as well as to provide a clean layer to place a 5lb 76mm x 76mm x 25.4mm steel block on top of the bonding area to hold it in place over the two-hour curing cycle. Because the resin was not at B-stage at the time of bonding, the resulting test sample was placed onto the heating press at 180°C for another two hours to complete the cure.

An addition to the original method for bonding the test samples was implemented in this study. First, the B-staged resin was poured around the defect. Second, the borders of the bond-line area were covered by four strips of ABS approximately 30mm by 1mm by 1 mm volume to function as a barrier to avoid resin leakage and thickness irregularities. Third, the half-made sample was put into a vacuum oven at 120°C and -0.90 MPa until bubbles surfaced on the bonding area. Fourth, the assembly was removed from the oven and placed on an aluminum plate cooled to -18°C to increase the viscosity of the resin for more time to manipulate the borders if they shifted in the heating. Fifth, the top CFRP/ZTCFRP coupon was placed onto the assembly in a side-to-side motion to further reduce the chance that air pockets would form. Sixth, the regions outside the

bond-line region were coated in parchment paper layered with Kapton tape. This would prevent any of the resin which leaves the bond-line from curing onto the regions, reducing surface finish irregularities which would affect the thermogram. The entire bond-line region was held in place by a frame. The top and bottom coupons held the ABS strips in place during curing. Lastly, the sample is wiped down with acetone in the direction away from the bond-line region to avoid contaminating the sample. Wiping the excess resin from the sample has the benefit of creating a more homogeneous surface thermal and electrical conductivity for the CCFRP/ZTCFRP coupons, which was an issue in the CNF defect thermograms in the preceding study. It is also important to note that the placement of the sample determines where the excess resin would pool during curing. Therefore, the sample was placed as level as possible inside the oven to reduce the chance of thickness irregularities and resin pooling. Sample bond-line thicknesses would be measured after curing and subtracting the original coupons' thickness from before they were bonded together. The bond-line resins used in this part of the study were comprised of one year old, but still well-preserved and useable, 1wt%, 2wt%, 3wt%, and 4wt% ACNT. Additional stock of these resins was needed once the old stock was used up. A master batch of 3wt% ACNT master-batch enriched epoxy was made in response. The newly made resins were not sonicated, however. This was out of fear of damaging the ACNT and possibly harming the electrical conductivity of the bond-line samples. Additionally, the master-batch manufacturer's instructions do not include sonication as part of the resin preparation.

### 3.3.2 Preliminary bond-line resin QCs

As stated in section 3.2.4, the resins used for the bond-line were made from a 4wt% master batch which was then diluted into equal amounts of 1wt%, 2wt%, and 3wt% ACNT. Samples were taken for microscopic analysis. The resins reused from the preliminary study are denoted as conference batches in the Figures listed below.



Figure 9: 4wt% to 1 wt% ACNT, conference batch, 100x.

Notice how there are agglomerations in Figure 9. This is primarily due to the limitations of processing equipment at this current time. The HSM step required a 5000 rpm for 30 min to completely disperse the ACNT throughout the resin matrix. The fastest spin rate available was nearly a tenth of that so further processing could not proceed without sonication or a surfactant side study.

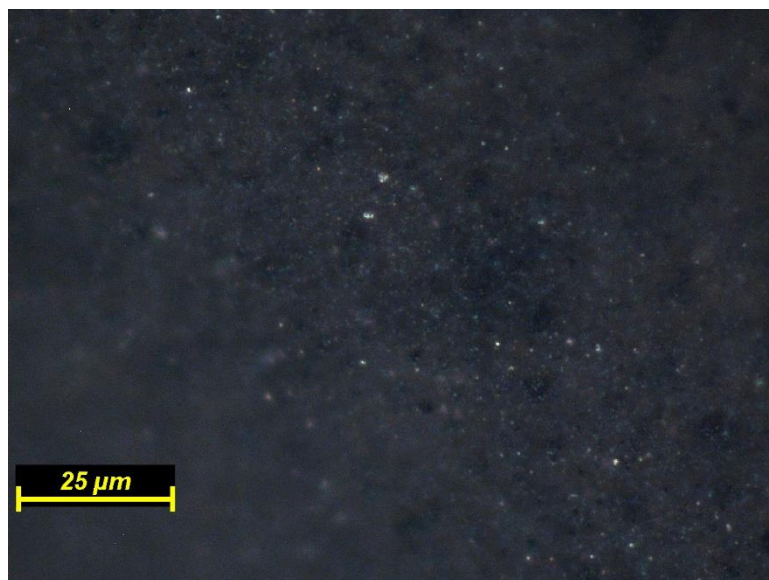


Figure 10: 4wt% to 1wt% ACNT, conference batch, 1000x.

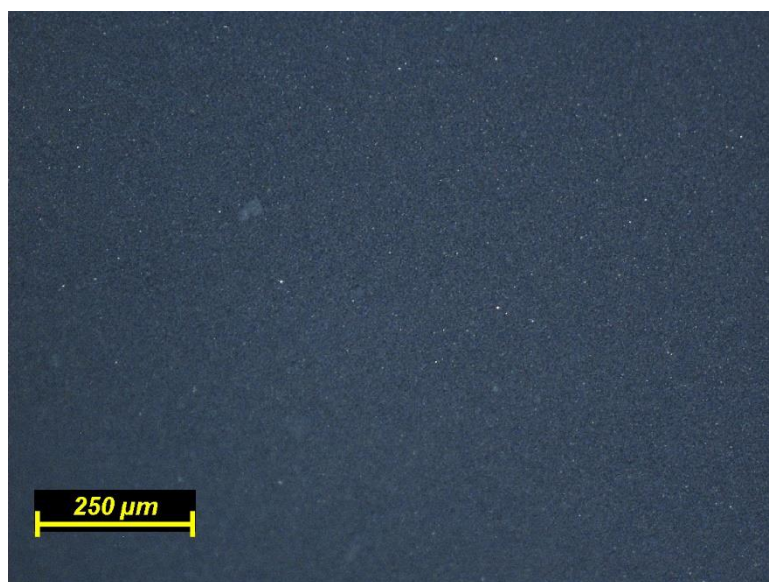


Figure 11: 4wt% to 2wt% ACNT, conference batch, 100x.



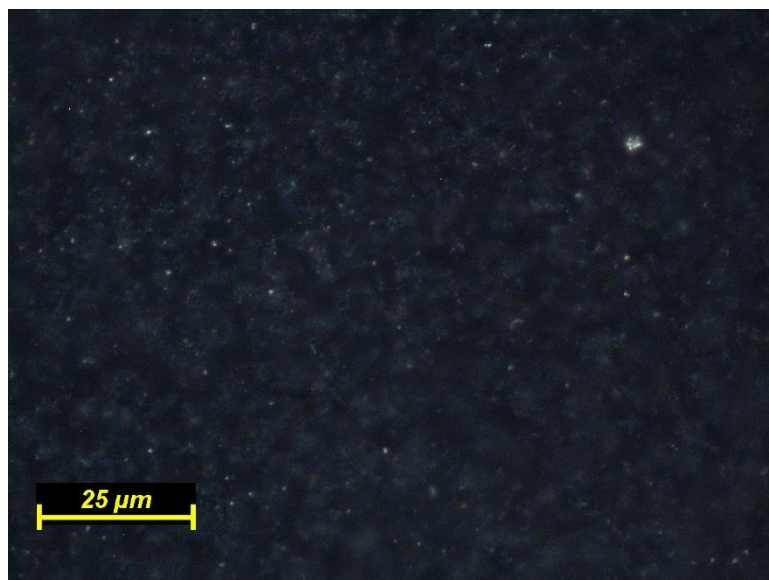


Figure 12: 4wt% to 2wt% ACNT, conference batch, 1000x.

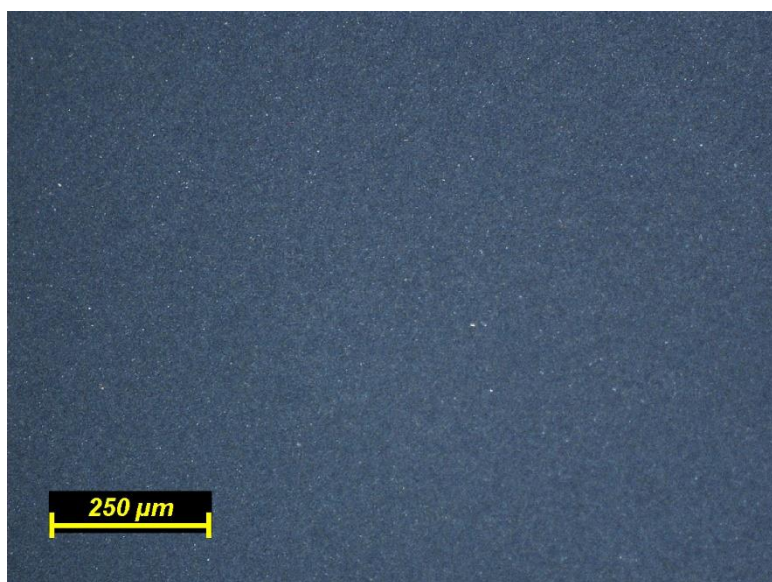


Figure 13: 4wt% to 3wt% ACNT, conference batch, 100x.

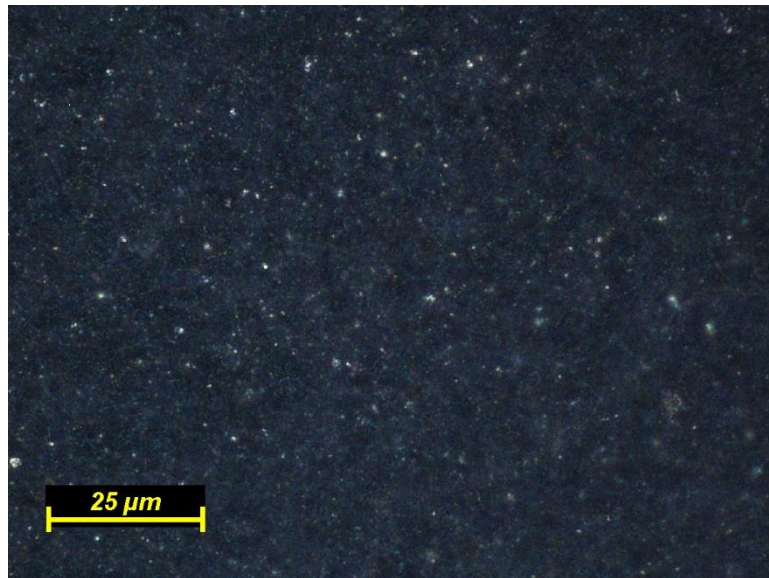


Figure 14: 4wt% to 3wt% ACNT, conference batch, 1000x.

### 3.3.3 Investigative bond-line resin QCs

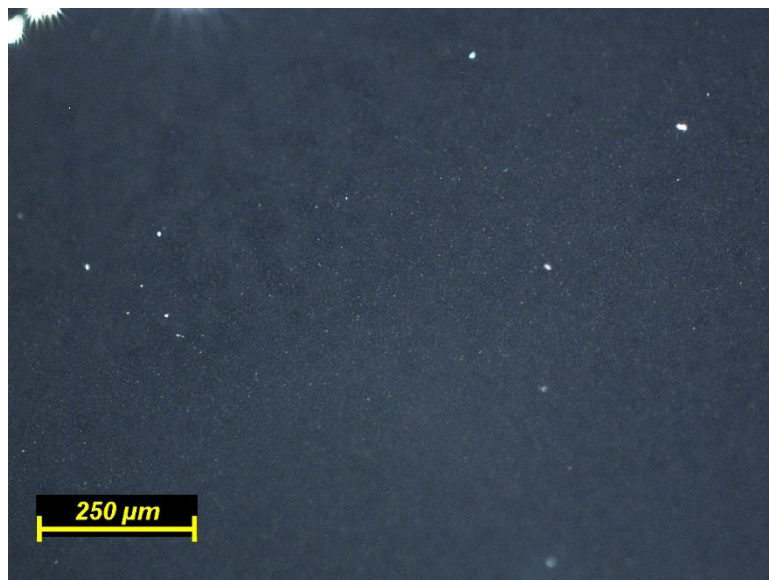


Figure 15: 4wt% to 2wt% ACNT, 4 hours HSM, remade batch, 100x.

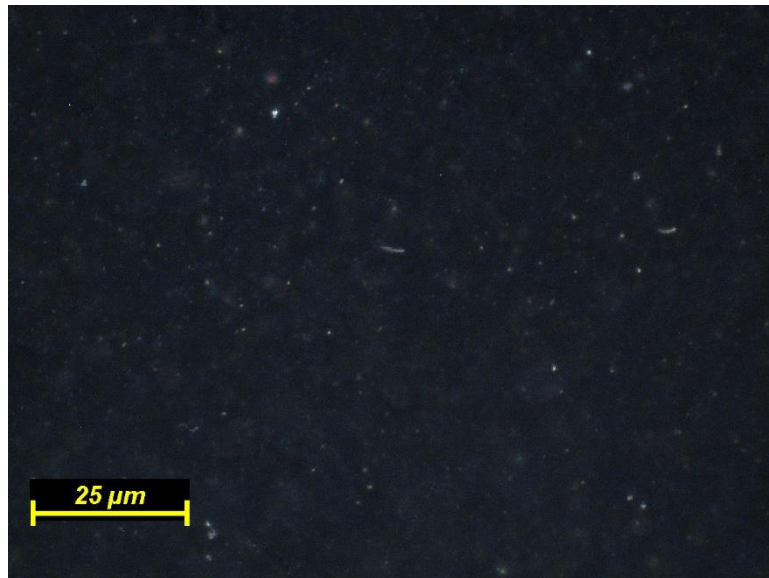


Figure 16: 4wt% to 2wt% ACNT, 4 hours HSM, remade batch, 1000x.

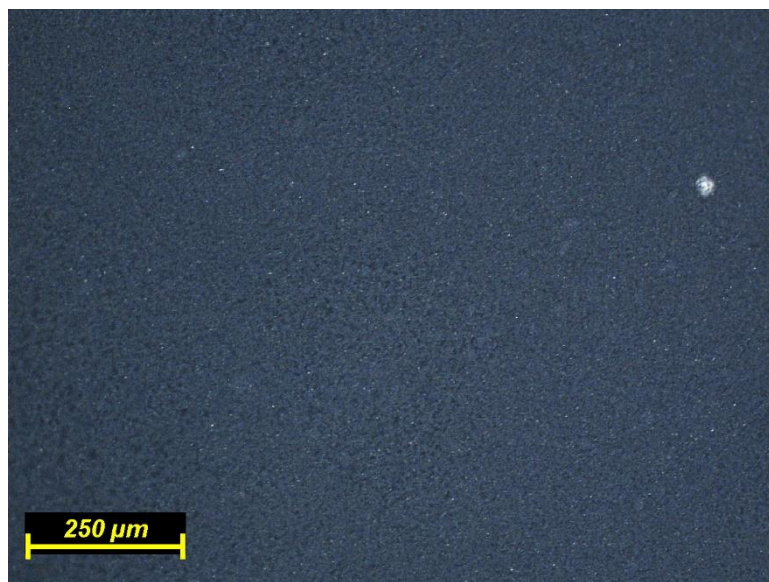


Figure 17: 3wt% ACNT master batch, 1 hour HSM, remade batch, 100x.



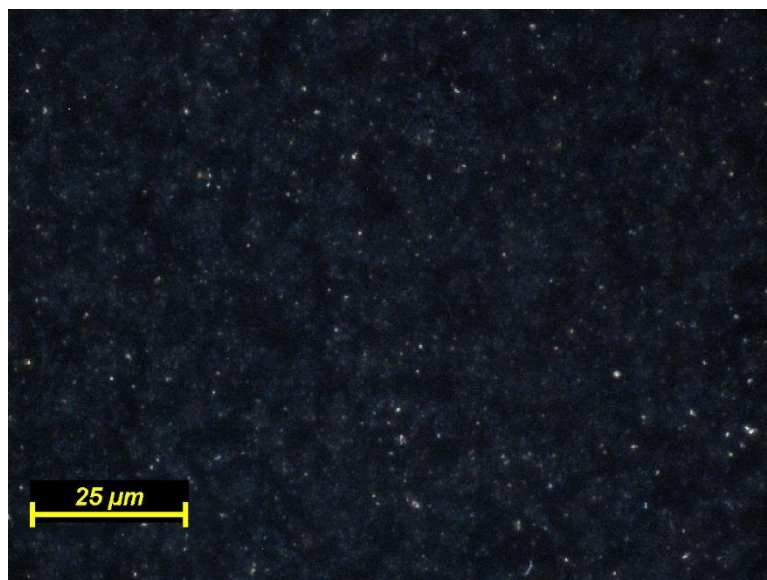


Figure 18: 3wt% ACNT master batch, 1 hour HSM, remade batch, 1000x.

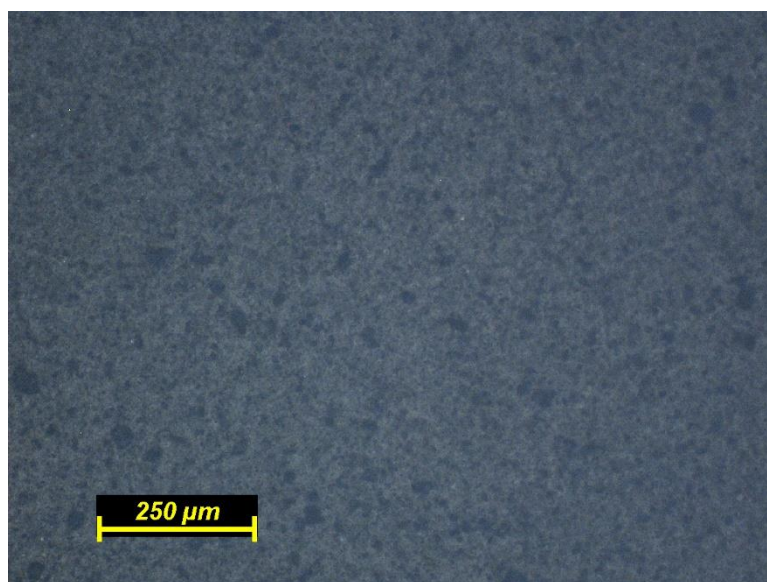


Figure 19: 3wt% ACNT master batch, 4 hours HSM, remade batch, 100x.

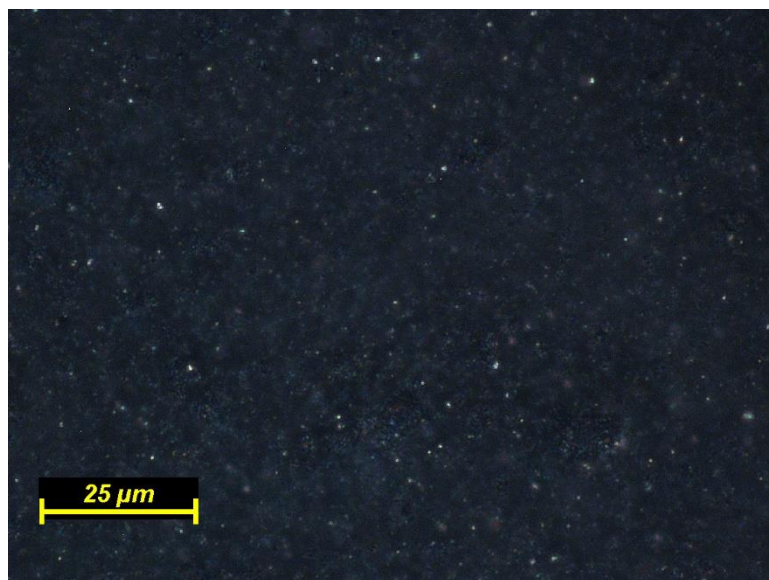


Figure 20: 3wt% ACNT master batch, 4 hours HSM, remade batch, 1000x.

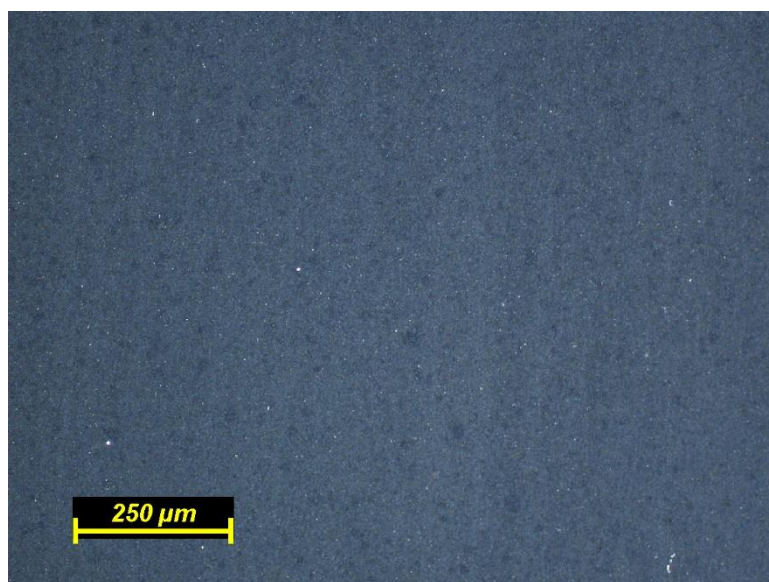


Figure 21: 3wt% ACNT master batch, 4 hours HSM, 1 hour sonication, remade batch, 100x.

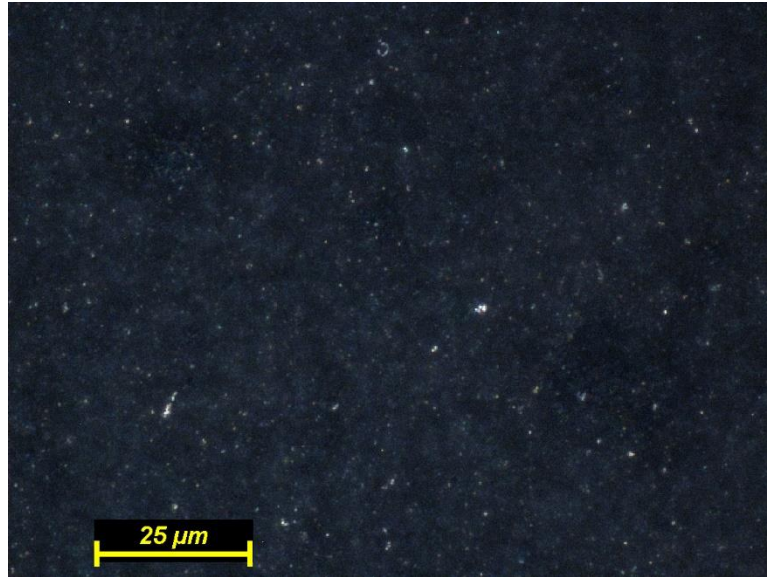


Figure 22: 3wt% ACNT master batch, 4 hours HSM, 1 hour sonication, remade batch, 1000x.

It is apparent that the quality of the remade batches suffers due to the absence of sonication. Efforts to further disperse the ACNT were to increase the rotation rate and HSM processing time. This outcome is supported from literature where researchers investigated methods to disperse the ACNT when mass producing epoxy-based composites. Their study focused on the mechanical and electrical properties of cured resins of ACNT and the impact which different dispersion methods have on them. They high shear mixed the ACNT, hand-mixed the ACNT, and used a three-roll mill on the ACNT as part of the comparison study. A three-roll mill is a piece of equipment used to disperse agglomerates of a nanomaterial by passing them through a series of rollers which imposes shear force on the material [28]. The overall quality found in the images above is surprisingly sufficient, even one year later. In order to be thorough, a portion of the freshly made 3wt% ACNT was sonicated for an hour to match the conference paper's

3wt% to determine if there was any change in electrical resistivity between the new batch and the old batch.

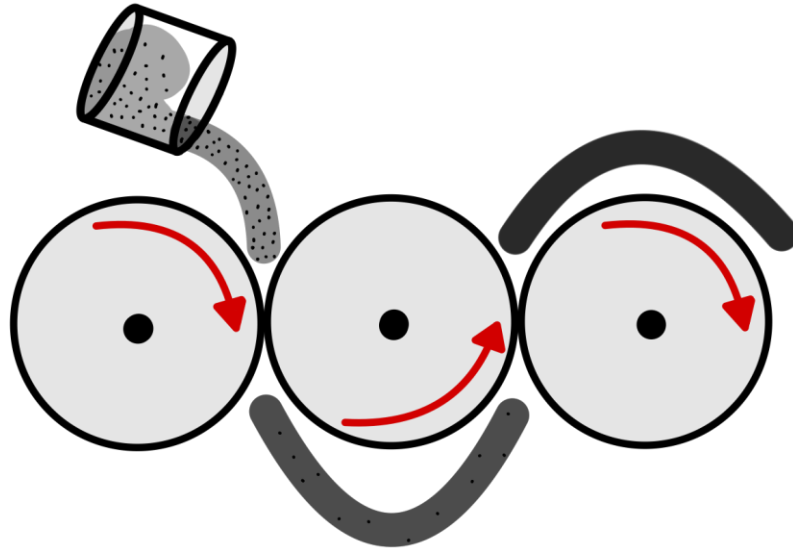


Figure 23: Visual representation of an epoxy-CNT mixture undergoing three-roll milling. The level of agglomerations decreases while the level of dispersion increases as the resin undergoes this processing.

### 3.3.4 ZTCFRP-prepreg manufacturing

Previous studies around ZTCFRP have used lower areal weighted carbon fabrics such as AS4 (190 GSM), and AS7 (190 GSM). T700s, however, boasts an areal weight of 680 GSM. The densities of these CF fabrics are 1.79 g/cm<sup>3</sup>, 1.79 g/cm<sup>3</sup>, and 1.80 g/cm<sup>3</sup>, respectively. As these CF fabrics share a nearly identical density, this shows the fabric thickness of T700s is much more than AS4 and AS7. Previous methods of thin resin film impregnation into CF such as the hand-layup method used in the preliminary study would

not be viable for making ZTCFRP as the arrangement of CNF would be disturbed and lose its alignment before it could be made into the much thicker CF fabric.

Efforts were then redirected into creating a prototype prepreg pressing tool which would both save time and labor, as well as save OOVBO materials for later use for curing. Two plates, which heat CF and cool aligned film, impregnate the carbon fabric with the melted resin and CNF z-threads. These plates allowed a tight control on the inlet and outlet height to manipulate the output prepreg's FVF. A visual description of this design is described in a published patent application [29]. The further details of this design and operations are proprietary to the Hsiao research group and will not be discussed here.

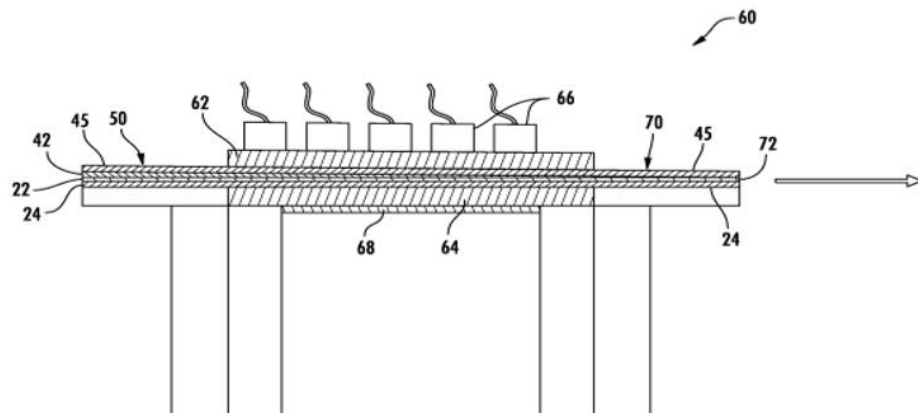


Figure 24: Prepreg compression plate. Hot CF is fed through the inlet while being topped with the ZT-Film which is then cooled by fans on top of the plate and then extruded as prepreg at the outlet. (Use of illustration from [29] was granted.)

After passing through the press plate assembly, the resulting prepreg's thickness was measured to compare to the desired thickness to match 60% FVF. If the prepreg was

thicker than desired, a film coater with a gap thickness of 0.63 mm or 630 microns (thickness for 60% FVF for a composite made with T700s carbon fabric) was heated in an industrial heating press to 120°C. After reaching the desired temperature, the thicker prepreg was passed through this gap to compress it to a FVF of 60%. The ZTCFRP samples were compressed by this method to remain at a relevant FVF to that of the control CFRP samples. The ZTCFRP prepreg made without this additional compression yielded an average FVF of 49.3%, while the control CFRP was 61.3%. The importance of uniformity of FVF between both ZTCFRP and CCFRP was to allow previous findings using 60% FVF to be compared more comprehensively. However, the thermal conductivity of both CCFRP and ZTCFRP have been modeled in previous research which was used to estimate the values for the samples manufactured.

In this investigative study, this prepreg method was used to create 6in by 3in T700s ZTCFRP coupons for testing. The process of making the bond-lines in the preliminary study was used again to create 1wt% CNF resin film for the ZT-prepreg. For a more robust dataset, each of the ZTCFRP and CFRP coupons were measured for their dimensions and densities for later calculations.



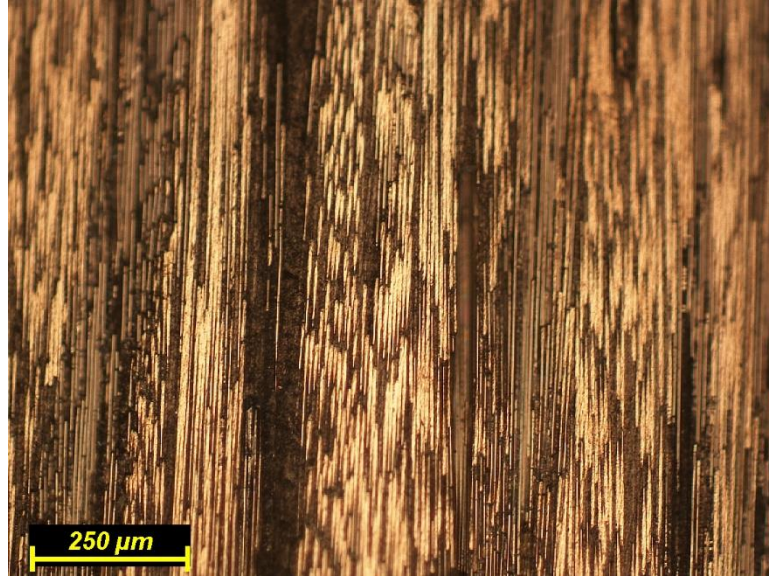


Figure 25: Image of 4 plied T700s 1wt% CNF ZTCFRP, 100x.



Figure 26: Image of 4 plied T700s 1wt% CNF ZTCFRP, 1000x. The yellow circles show the CNF facing the Z-direction perpendicular to the CF direction.

Due to the difficulty in making it, the edges of each ply are visible whereas a higher quality ZTCFRP would have little to no visible border.

### 3.3.5 OOA-VBO modification

In the last study, the CFRP coupons were cured through the OOAVBO process listed in Figure 27. This method allowed for a consistent FVF throughout testing. However, a different style of OOAVBO was used in the investigative study, as it yielded a very smooth surface on the prepreg used for bonding. These changes saved time from sanding the CFRP coupons which was the deciding factor for making this change.

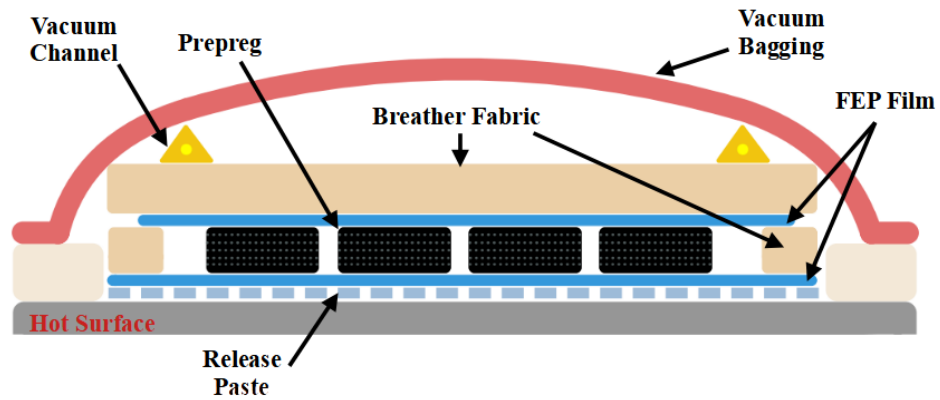


Figure 27: Modified OOA-VBO process.

Note the absence of a breather layer beneath the prepreg. This was left out to preserve the smoothness of the underside. FVF and QC examinations were conducted to ensure the CFRP panels were test-worthy.

### 3.3.6 Defect depth analysis

As stated before, IRT has limitations to how deeply it can detect internal defects within a composite. The experiment comprised of two sets of CFRP: three samples of CCFRP with one, two, and four plies thick per coupon, and three samples of ZTCFRP



with one, two, and four plies thick per coupon, respectfully. A seven-ply thick test sample made of ZTCFRP was considered to verify that the quality of the defects' thermogram would be the approximately the same as a one ply thick test sample made of CCFRP. This is due to the thermal conductivity of ZTCFRP being 7.53 times that of CCFRP [19]. This was not pursued as even four ply T700s ZTCFRP proved almost too difficult to make.

### **3.3.7 Bond-line electrical conductivity consistency study**

The electrical conductivity of the bond-lines plays a greater role than that of the thermal conductivity of the bond-line based on direct comparisons of ZTCFRP and CCFRP. For consistency as well as a chance for more accurate readings, the EC was measured once more, although this time under more scrutiny. One weakness of the last EC tray design was the inability to verify whether the bond-line between the copper plates was in complete contact with them as well as whether air pockets were present. Additionally, the two-probe method used in the previous study was deemed ineffective, as the contact resistance of the epoxy would still influence the reading. A four-probe design was created to allow direct view of the bond-line as well to allow the air pockets to dissipate more readily while degassing with a larger gap of 14.5mm in comparison to the preliminary design's 1mm.

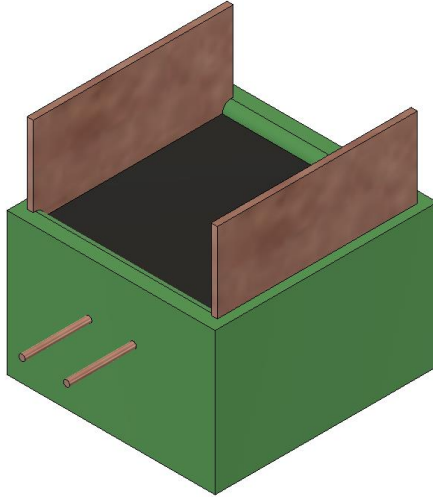


Figure 28: Four-probe tool for measuring the electrical resistivity of the bond-line resins.

The calculation of electrical conductivity is similar to the manner used in the preliminary study with the exception of using four-probe instead of two-probe measurement. The direct current ( $I$ ) flows in series across the cross-sectional area ( $A$ ) of the sample's electrodes and the input voltage ( $V_1$ ). The voltage drop ( $\Delta V_1$ ) across a resistor ( $R_1$ ) as well as the voltage drop ( $\Delta V_2$ ) across the two parallel copper wires with a gap distance ( $d$ ) are measured to calculate the electrical resistivity of the resin.

$$\sigma = \frac{I d}{\Delta V_2 A} \quad (7)$$

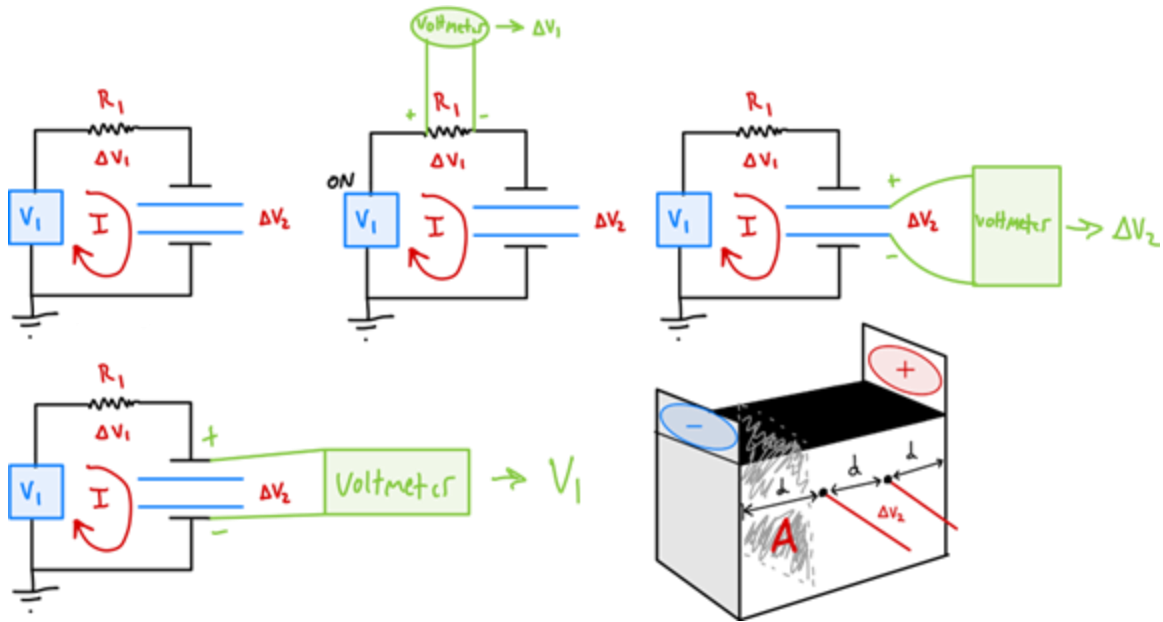


Figure 29: Basic four-probe electrical resistivity tool wiring schematic.

### 3.3.8 Computer aided IRT

The tuning of the infrared camera plays a significant role in determining the quality of the resulting thermograms. The recording parameters for the IRT measurements for the investigative study were kept the same as the preliminary study's configurations. In previous tests, the range of temperature of the bond-line area was controlled automatically to provide the user with a consistently clear view of the defect and bond-line. This procedure overlooked an important aspect for thermography as it lessened the drastic gradient in temperature where the defect and conductive resin begins. This change in temperature allows the defect to be seen clearly. This is an obvious statement although the implications are significant. As the auto-scale detects the difference in temperature, it artificially raises the upper range of temperature and obscures the clearest possible defect image.

To rectify this past mistake, the imaging procedure was constrained to a set temperature configuration range for all cases. The recorded video was placed into a post-processing image software, Flir's ResearchIR, to analyze the raw image data after testing. This software allows post-processing of thermograms after the initial recording. The power was applied at the same time when recording the raw data, so the temperature profile of the sample was also collected over the course of one minute. For post-analysis, the temperature range for the modified thermogram recording was the peak temperature in the set of 900 frames for the upper bound and the minimum temperature in the initial frame as the lower bound. The clearest and most contrasting frame was picked to be analyzed with the adjusted temperature scale. This distinction was based on a visual analysis of each of the 900 frames which could be played as a video file. This procedure is described in detail in Appendix B.1.

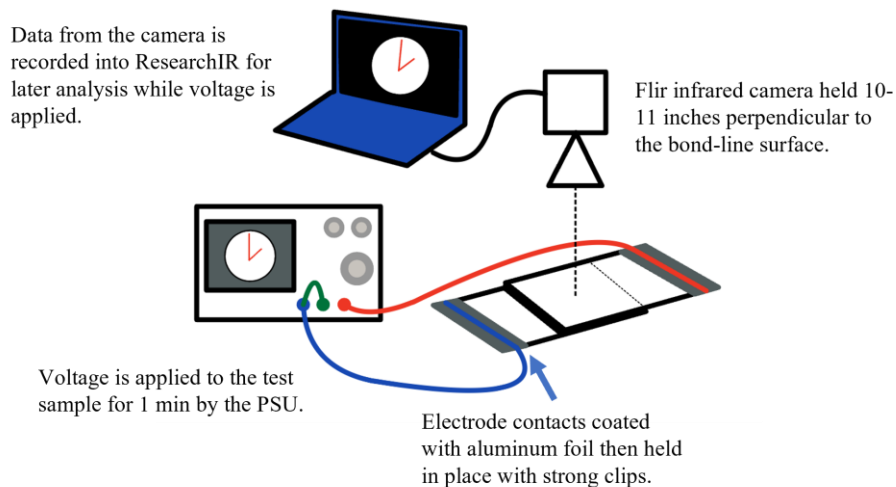


Figure 30: Computer aided IRT setup.

Clamps fix the electrical contacts onto the surface of the sample while the bond-line area warms from JH. The resulting information is recorded on a computer for later analysis. One point to note is that a defect template was placed on the outer surface of the bond-line area to allow a visual sense of scale for post-processing the raw data in the recording. This defect template was made of ABS as well and conforms to the defect's shape, area, and thickness. It does, however, differ in one respect in that it is hollow in the middle so that only the one mm thin triangular perimeter is shown. This is to avoid obscuring the resulting thermogram with a template with a large area to heat to thermal equilibrium.

Additional effort was put into making better electrodes in this study. In the preliminary study, the contacts were held in place with unwieldy vice grips. This new design used aluminum coated gasket tape as well as aluminum foil to contact the top and bottom of the CFRP as well as the side touching the unidirectional CF. This would allow a better contact for current to flow into the sample. Kapton tape was used to prevent outside interference and the bases were 3D printed with PLA filament which further reduced the impact on the imposed current flowing into the sample. Strips of aluminum leftover from the preliminary study were reused to function as attachment points for the current to be imposed. The whole assembly was held together by Kapton tape and large office paper clips which tightly secured the sample during testing.

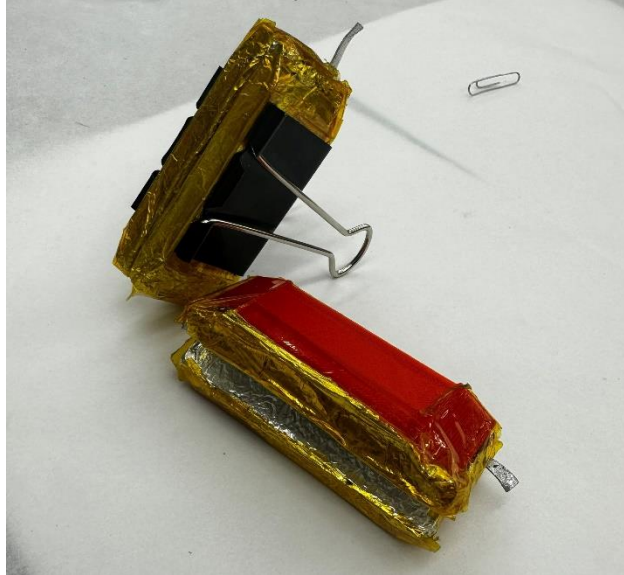


Figure 31: Improved electrode contacts for JH-IRT.

### **3.3.9 Bond-line uniformity study**

Initially, the first reaction to seeing the thermograms having darker spots where they should not be directed effort into checking the bond-line resin's Tt.E.C. Results from these tests were inconclusive as an outlier was present inside the samples taken from each wt% sample batch. Further analysis has shown that the sealing of the bond-line prior to curing was the main source of the inconsistent bonds.

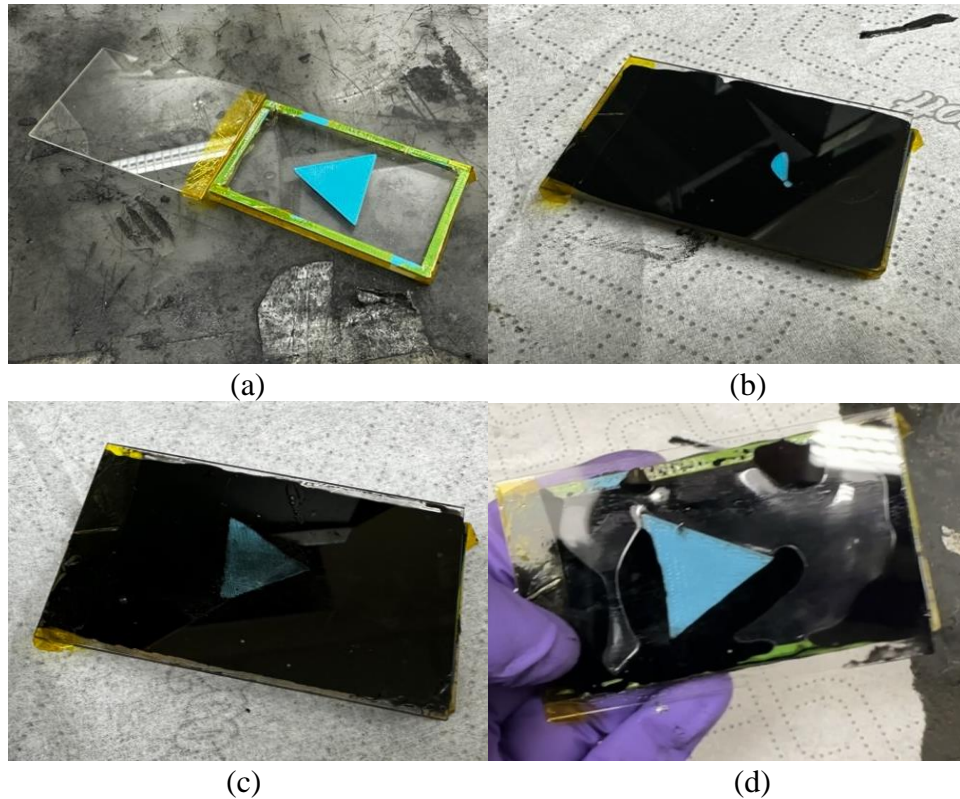


Figure 32: Bond-line consistency test. (a) Bond-line resin flow tool, (b) no resin covering top or bottom, (c) resin covering top but not bottom, (d) false positive scenario where resin either leaks out or improperly filled although seems fully loaded with resin.

The method of closing the top coupon such as those shown above was not extensively documented as the bond thickness at the time of curing appeared sufficient to completely cover the bond-line area. From the resulting thermograms, scenarios c and d are visible. Scenario d shows the incomplete sealing through the glass sheet although invisible to the technician. Following these discoveries, further cases were bonded with excessive resin to further reduce the chance of air pockets. Later in the analyses, it was hypothesized that the reason some samples had air pockets, other than the lack of adequate resin, were subtle differences in thickness of the CFRP and ZTCFRP panels,

resin dams, and the defect. This difference in the bond-line gap and the bond-line thickness could be enough to allow air pockets to form.

### 3.3.10 F-IRT setup

While considerable effort was devoted to avoiding air pockets from forming within the bond-line, they were present in some test samples for this part of the study. However, pairing another method of IRT, F-IRT, with the JH-IRT method, the regions of colder temperatures can be overlaid from both methods. This pairing attempts to differentiate between air pockets and the intentionally placed defect. As the ABS defect has a higher thermal conductivity than that of the air within the bond-line, the defect area will reach thermal equilibrium faster than the air pockets. The testing setup is explained in Figure 33.

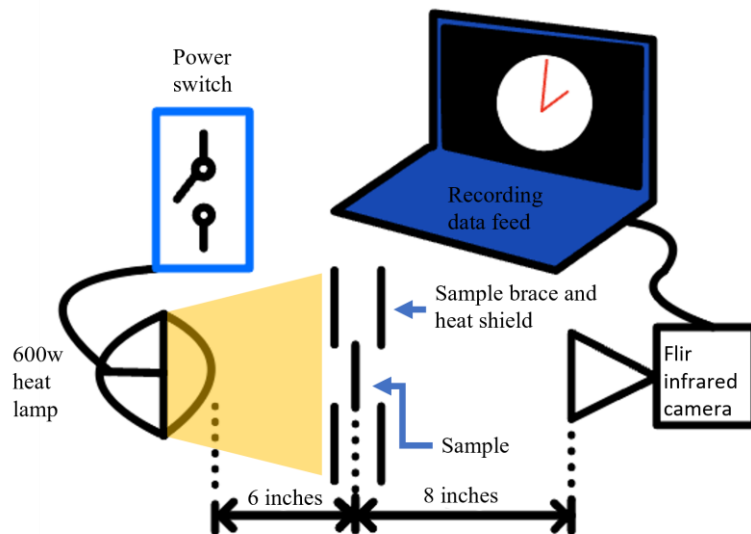


Figure 33: F-IRT testing setup. The lamp was turned off manually with the aid of a stopwatch.



The estimated heat flux onto the samples should be consistent due to the placements of the infrared camera, the thermal shield containing the sample, and the 600W halogen lamp remained as undisturbed as possible. The thermal shield would change position slightly when loading the next sample. The outline of the lamp, sample shield, and camera was drawn onto the workbench, allowing any misalignment to be fixed before the next measurement. The time span where the lamp would heat one side of the sample was kept as close to five seconds with the help of a stopwatch. This exposure time was lengthened from the recommended time of five milliseconds to five seconds. The reason was due to the absence of a testing array to switch the power on and off electronically. The risk of more measurement error was compounded due to physical limitations to switch the lamp on and off in consistent spans of time. This was the reason five seconds was chosen over one second as the variance in exposure times would be less than the one second time span.

### **3.3.11 Defect image grading**

While the similarity between the defect image and the defect template is important, contrast, shape, wattage applied, as well as the span of time to see the defect are all together present in a quality thermogram. Contrast can be described as the difference in light intensities inside an image. As an infrared camera displays incoming infrared radiation into visible wavelengths of light, the color scheme of an infrared camera can be adjusted for many applications. For this study, the ‘fusion’ color palette was chosen as it displayed defects more clearly. The fusion palette is a preset modification of the ironbow palette in which the temperature scale favors higher temperatures which means more of the color scale is influenced by higher temperatures.

This could be a way for subtler temperature differences to be displayed rather than an even distribution of colors which is found in the ironbow palette. This scale ranges from deep purple to white, corresponding to colder and hotter regions. The difference in color can be described as the temperature gradient. Because the defect is not electrically conductive, it cannot transfer heat as well as its surroundings, resulting in a difference in temperature. The previous study has given credence that the more conductive the film adhesive, the larger the temperature gradient is.

The overall shape of the defects used in both studies are equilateral triangles of 30mm sides. In this study, a rudimentary quantification to the shape of the defect was made by measuring the distance of the shortest median line which was then used to calculate the area of an equilateral triangle of height equal to the measured distance. This calculated area was divided by the actual area the defect casts on the thermogram to make a ratio corresponding to the defect area that can exist inside an equilateral triangle. A ratio closer to one signifies the overall area of the defect is closer to the original shape of the defect as a 30mm sided triangle.

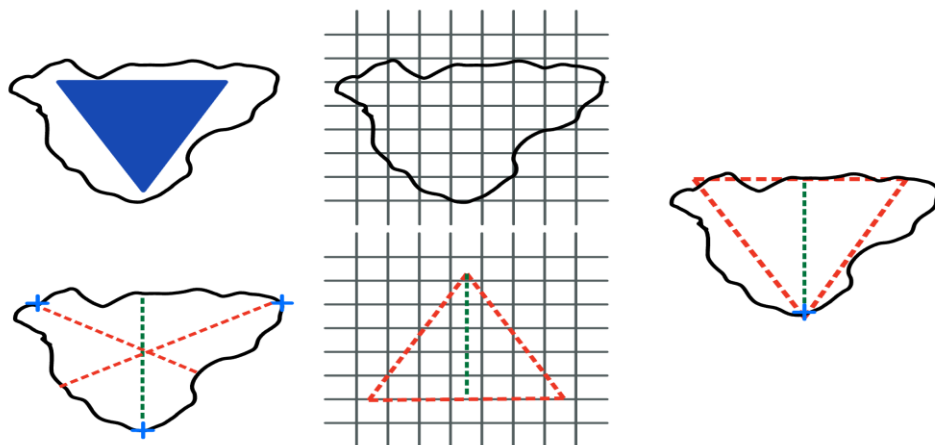


Figure 34: Rudimentary defect shape similarity process.

$$Shape_{similarity} (\%) = \frac{\frac{\sqrt{3}}{3}(Median_{Length})^2}{\Sigma Defect\ unit\ area} \quad (8)$$

The power applied to the bond-line and the resulting temperature difference can be related to the electrical conductivity of the bond-line. If all samples were free of air pockets or surface cured epoxy, this relationship could be better substantiated. A low power produces a starker contrast to see a defect is preferred in this context as it could be easier to view. The time span where the defect is visible is also an important detail for grading the thermograms. The longer the span, the more detail a technician could retrieve from an NDE test while in the field.

The grading criteria for this investigative study is the average value between the defect area and shape similarity parameters. Because they each a ratio less than one, they are normalized to one which means they are equally important. The grading scale for comparing every test case undergoing JH-IRT is listed below.

$$Grade (\%) = \frac{Defect_{similarity\%} + Shape_{similarity\%}}{2} \quad (9)$$

The grading scale for comparing useful defect time span between JH-IRT and F-IRT is listed below. Note this value is the ratio of the useful time and the entire time (sixty seconds).

$$Grade (\%) = \frac{Time_{Useful\ Defect\ time\ span}}{Time_{Entire\ recording\ time\ span}} \quad (10)$$

The reason two grading scales were used was because the comparison between JH-IRT and F-IRT was heavily in favor of JH-IRT. Some samples failed to even present a thermogram resembling the triangular defect for F-IRT. This also meant that the shape

similarity could not be calculated for every sample undergoing F-IRT. The common denominator for parameters between the IRT methods which could be reliably measured was the useful defect time span in which the defect was visible to the technician. The viewing time for JH-IRT was the full minute, while the viewing time for F-IRT was the span of time the defect became visible until it faded into the bond-line area.

## CHAPTER IV

### RESULTS

#### 4.1 Preliminary results

##### **4.1.1 Film adhesive tray Tt.E.C. assessment**

The Tt.E.C. measured from the ACNT/resin mixture cured in the tray setup and the ACNT/resin bond-line setup had a loose correlation to each other despite the same nanofiller concentrations (Figure 35). The tray study showed a weaker Tt.E.C. than that from the CFRP bond-line test samples. This can be from a variety of reasons such as: uneven bond-line thickness, partial cover of the film adhesive onto the copper panels in the tray prior to curing, resin shrinkage, or resin seeping into the probe terminals inside the tray obscuring the exposed copper plate prior to curing. These reasons could impact the overall Tt.E.C. measurements, especially for the tray study/setup.

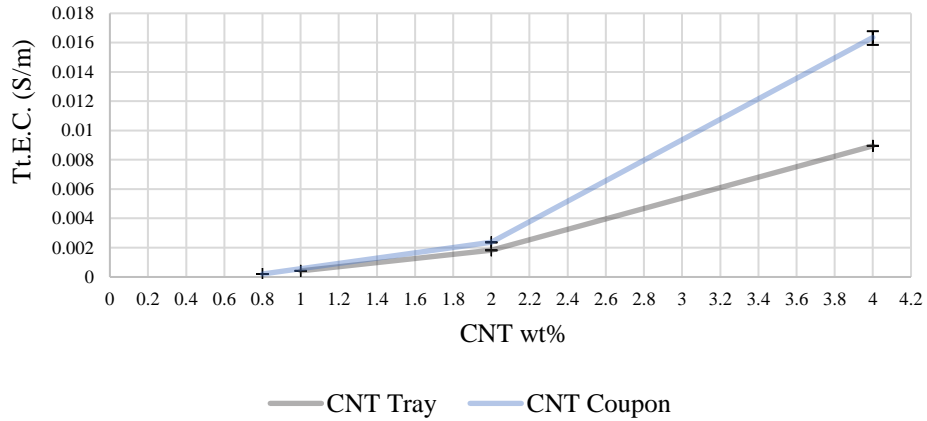


Figure 35: Comparison of the preliminary Tt.E.C. measurements.

In hindsight, the values above may have a large amount of uncertainty as the resistivity measurements were taken with the two-probe method.

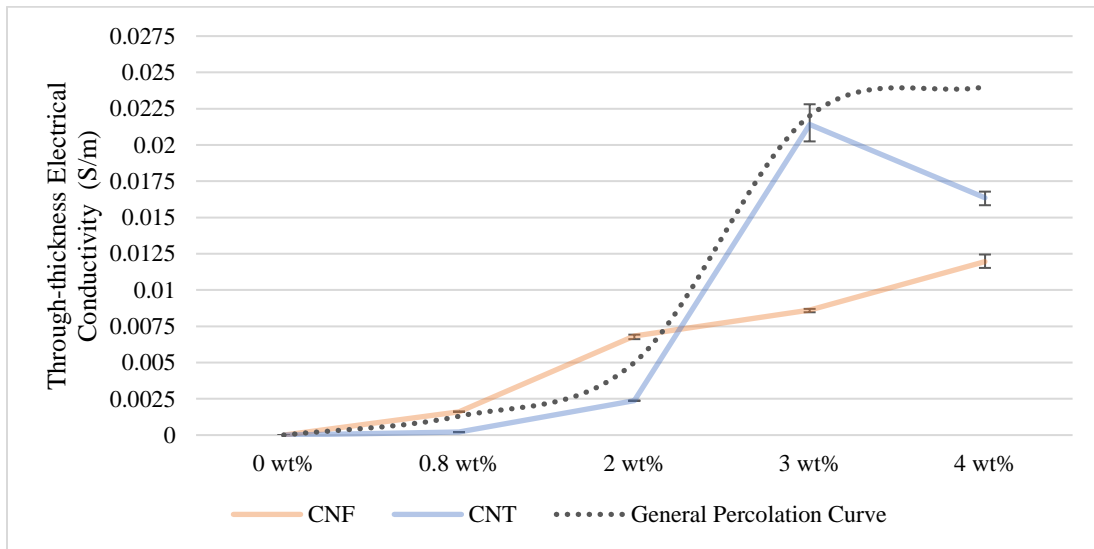


Figure 36: Preliminary Tt.E.C. comparison between CNF and ACNT bonded to CCFRP.

The ACNT trend appears to resemble the general trend of the percolation relationship with respect to the wt% of CNF and ACNT. The percolation threshold appears to be at 2 wt% for ACNT and at 0.8 wt% for CNF. The geometric aspect ratio of the nanofillers could explain this result. CNF has a diameter of approximately 100 nm and lengths of 50 – 200  $\mu\text{m}$  [30] and the ACNT used in this study has a diameter of  $\sim$  10-15 nm and length  $\sim$  0.10-10  $\mu\text{m}$  [31]. This difference in length and diameter can explain why more ACNT was needed to exceed CNF's electrical conductivity initially. The larger the surface area of the nanofiller, the more likely it is for the nanofiller to contact itself or the CF matrix. So, a nanofiller with a thicker diameter and longer length will outpace a nanofiller which is smaller and thinner in terms of the wt%.

#### **4.1.2 Preliminary thermograms**

Determining the scale of visual quality of the defects was considered after a comparison of all images. The following grading scale has been used to determine the visual quality of the defect image shown in the IRT imaging analysis below.

- 1. Triangular area visible: Edges and points are clearly visible.*
- 2. Triangular area visible: Clear edges, fuzzy points.*
- 3. Obscured visibility: Fuzzy edges and points.*
- 4. Hotspots: Cold areas have a semblance of defect.*
- 5. Hotspots: Cold area has no semblance of defect.*
- 6: No temperature change throughout the bond-line area.*

Figure 33.c and Figure 33.d show the clearest images of IRT results for the CNF/epoxy bond-line NDE tests and ACNT/epoxy bond-line tests, respectively. A constant voltage of 5V was imposed onto every sample and continuously recorded for one

minute. The CNF samples proved troublesome to read based on uneven bond-lines and exposed resin outside the bond-line, which formed after curing the test sample. All of these reasons could cause non-uniform JH across the bond-line and produce an irregular temperature signature.

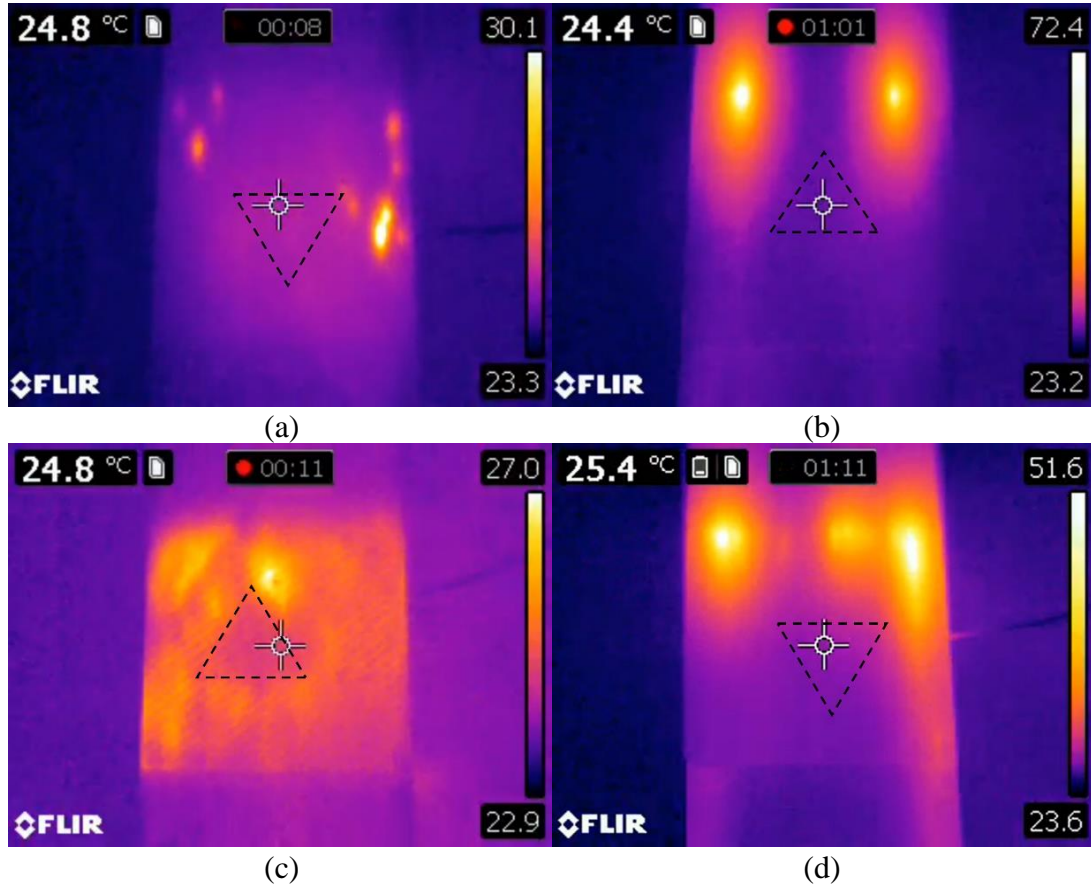


Figure 37: The CNF samples taken at the point of clearest image. The room temperature was approximately 22 °C. (a) 0.8 wt% CNF, (b) 2 wt% CNF, (c) 3 wt% CNF, (d) 4 wt% CNF.



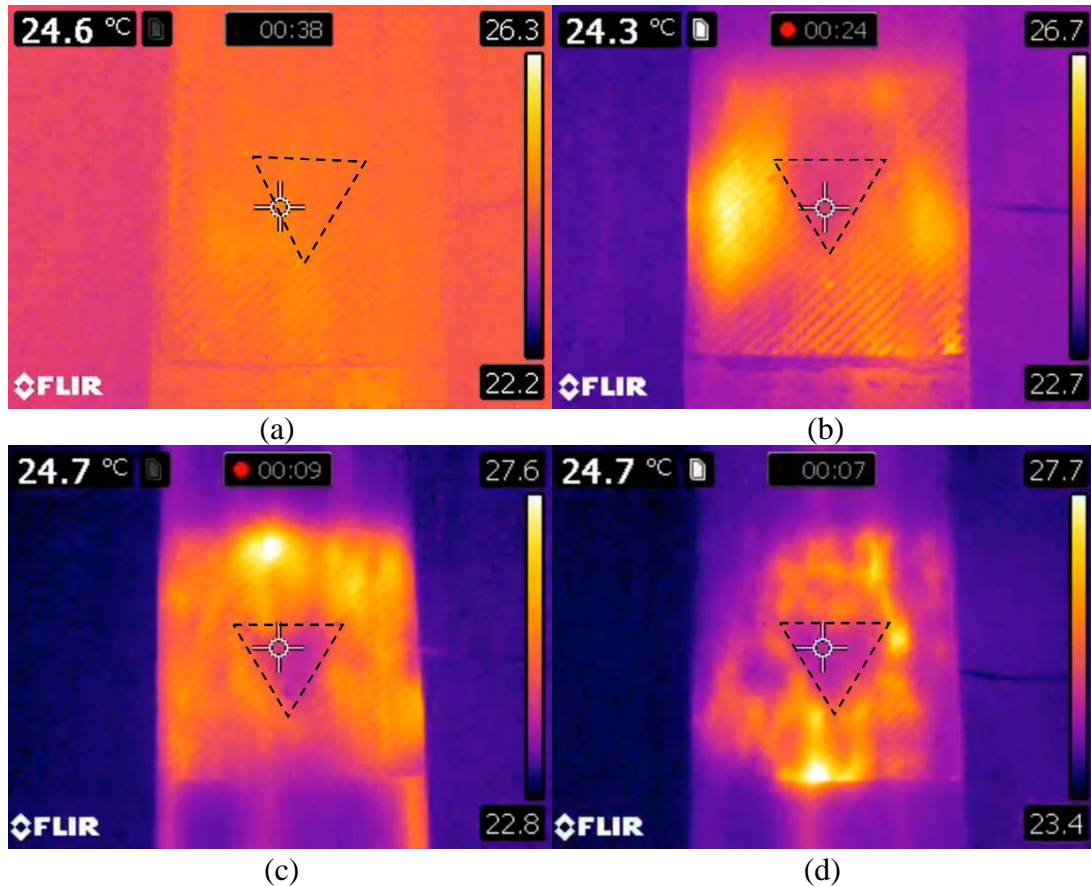


Figure 38: The ACNT samples taken at the point of clearest image. The room temperature was approximately  $22^{\circ}\text{C}$ . A constant voltage of 5V was applied to all samples. (a) 0.8 wt% ACNT, (b) 2 wt% ACNT, (c) 3 wt% ACNT, (d) 4 wt% ACNT.

## 4.2 Investigative results

### 4.2.1 Investigative thermograms

Constant voltage was applied to the CFRP and ZTCFRP coupons to invoke a JH response, similar to the preliminary study. The heat flux through the bond-line in these measurements were inconsistent when comparing IRT cases. The resistance, current, and power output values were recorded during the constant voltage study which were then used to find a power value each case could support through their bond-line. The defect

thermograms from the constant power approach were chosen to display the results. Additionally, the F-IRT results were displayed for a side-by-side comparison. Both CCFRP and ZTCFRP control bond samples had no reaction to the JH process so their mid-life frame, MLF, was used in absence of a visible defect frame.

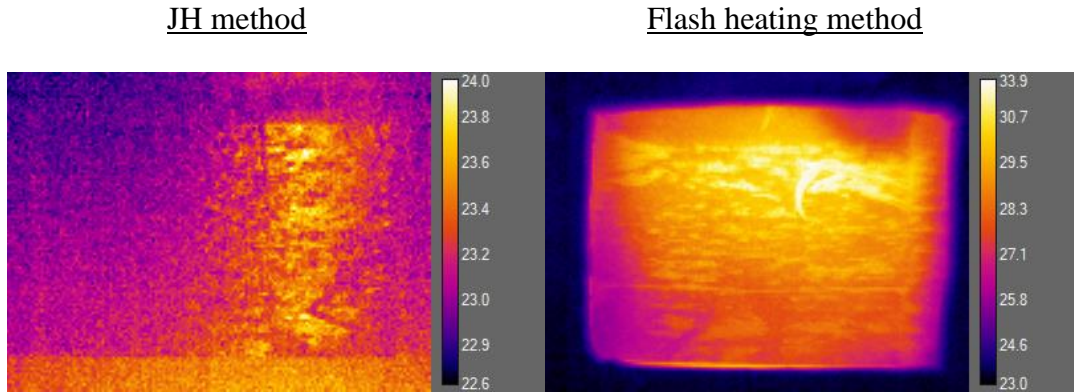


Figure 39: Control CCFRP 2p: at 30s (JH-IRT) and at 11.60s (F-IRT).

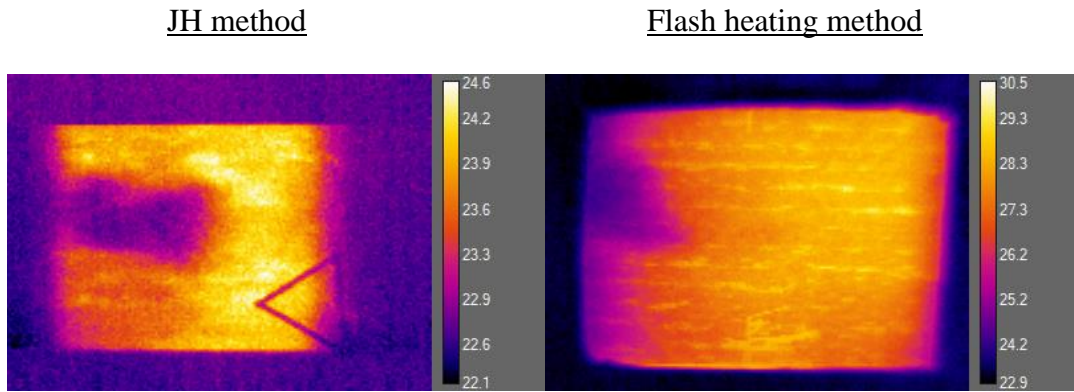


Figure 40: 1wt% ACNT CCFRP 2p: at 7.93s (JH-IRT) and at 8.13s (F-IRT).

JH method

Flash heating method

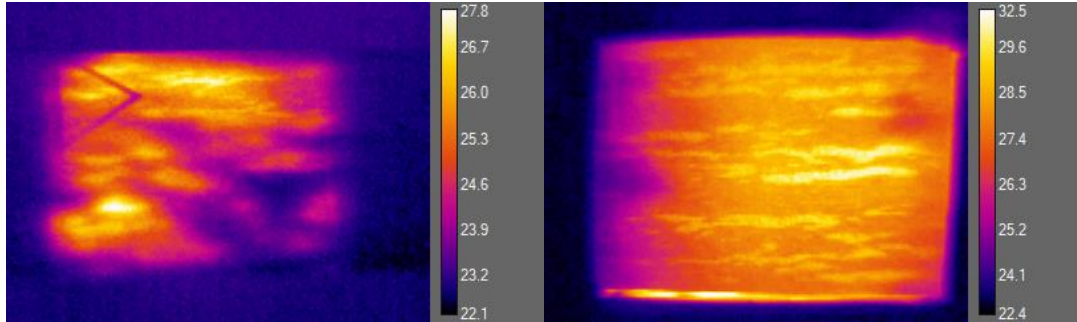


Figure 41: 2wt% ACNT CCFRP 2p: at 10.53s (JH-IRT) and at 11.40s (F-IRT).

JH method

Flash heating method

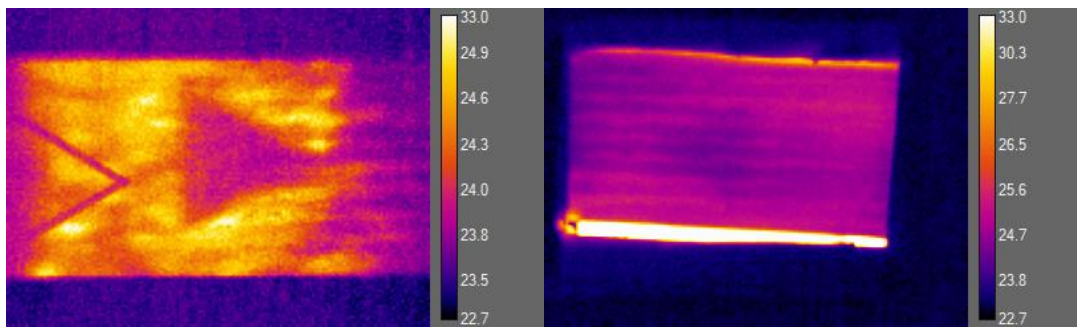


Figure 42: 3wt% ACNT CCFRP 1p: at 3.33s (JH-IRT) and at 6.07s (F-IRT).

JH method

Flash heating method

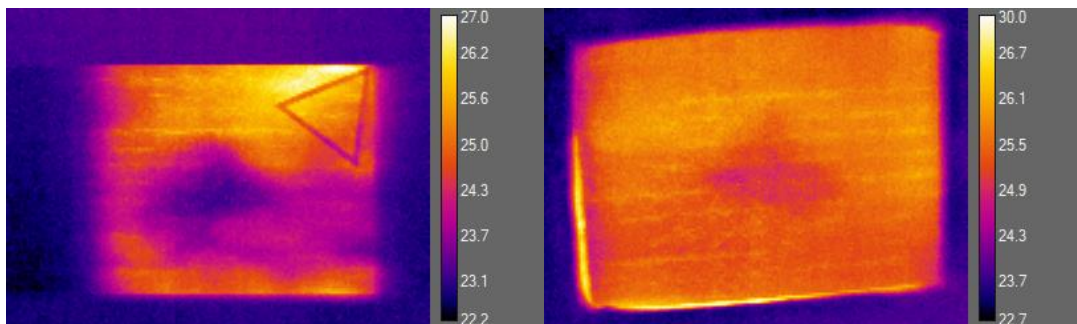


Figure 43: 3wt% ACNT CCFRP 2p: at 12.40s (JH-IRT) and at 6.80s (F-IRT).



JH method

Flash heating method

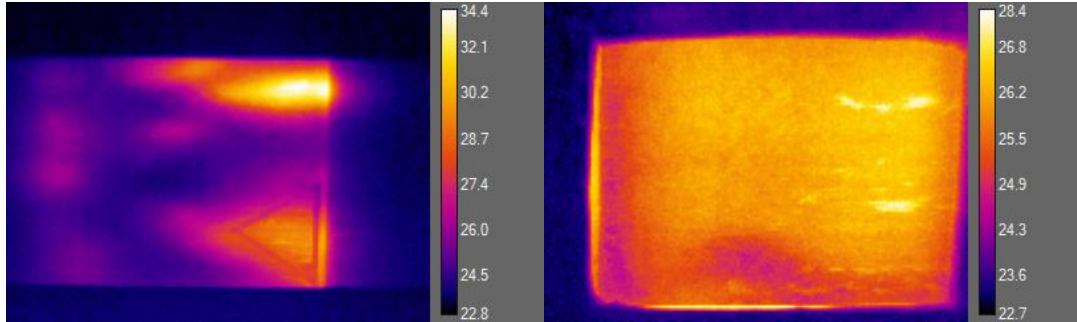


Figure 44: 3wt% ACNT CCFRP 4p: at 28.00s (JH-IRT) and at 18.47s (F-IRT).

JH method

Flash heating method

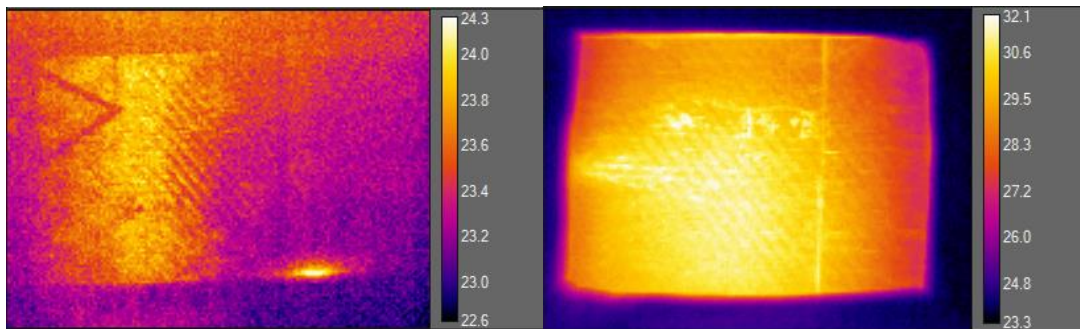


Figure 45: Control ACNT ZTCFRP, 2p at 30s, both cases.

JH method

Flash heating method

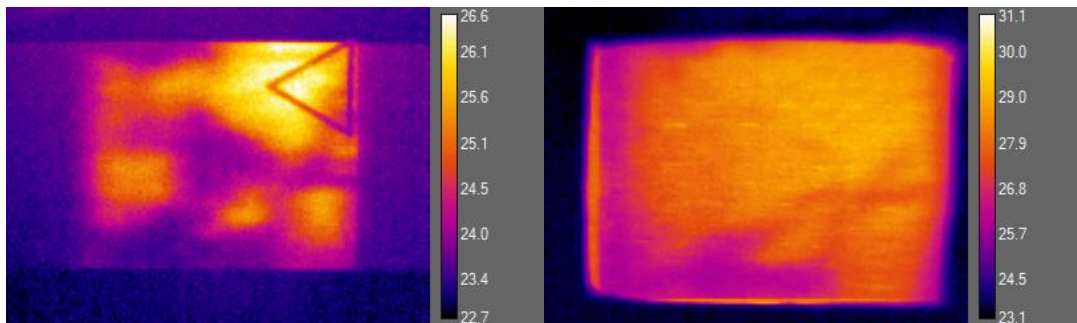


Figure 46: 1wt% ACNT ZTCFRP 2p: at 9.8s (JH-IRT) and at 13.9s (F-IRT).

JH method

Flash heating method

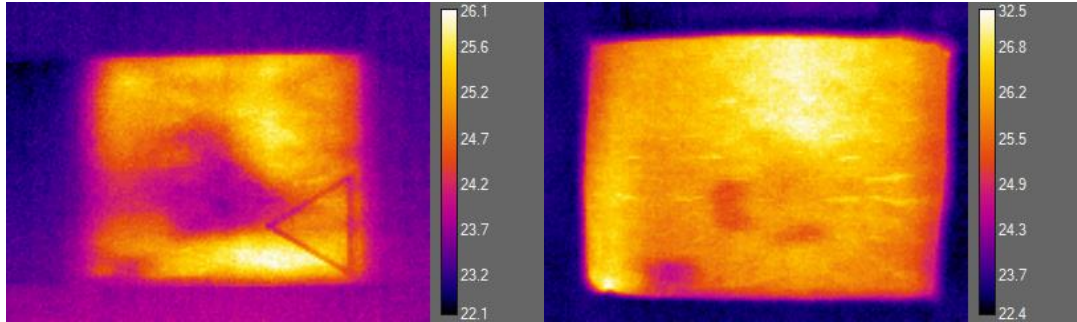


Figure 47: 2wt% ACNT ZTCFRP 2p: at 12.93s (JH-IRT) and at 9.13s (F-IRT).

JH method

Flash heating method

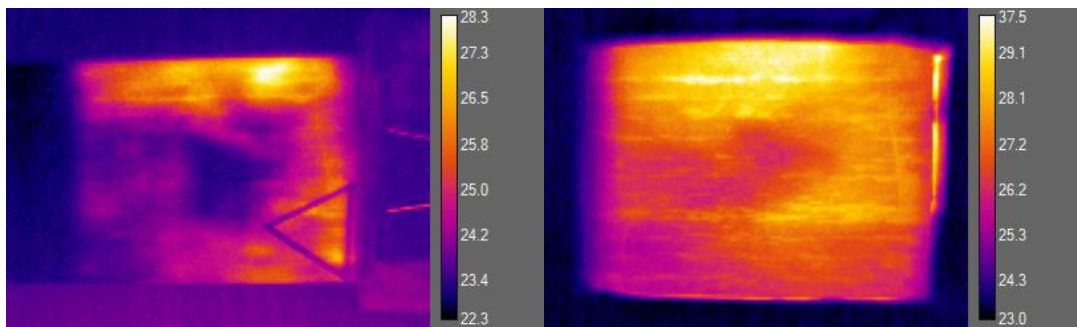


Figure 48: 3wt% ACNT ZTCFRP 1p: at 7.93s (JH-IRT) and at 5.87s (F-IRT).

JH method

Flash heating method

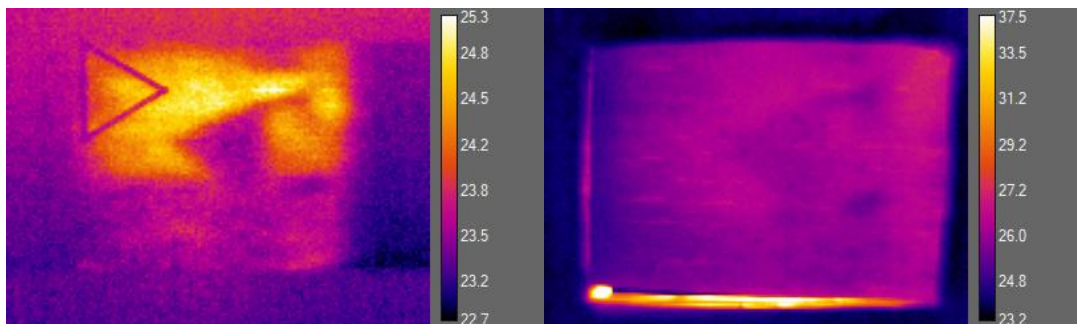


Figure 49: 3wt% ACNT ZTCFRP 2p: at 5.33s (JH-IRT) and at 8.87s (F-IRT).

### JH method

### Flash heating method

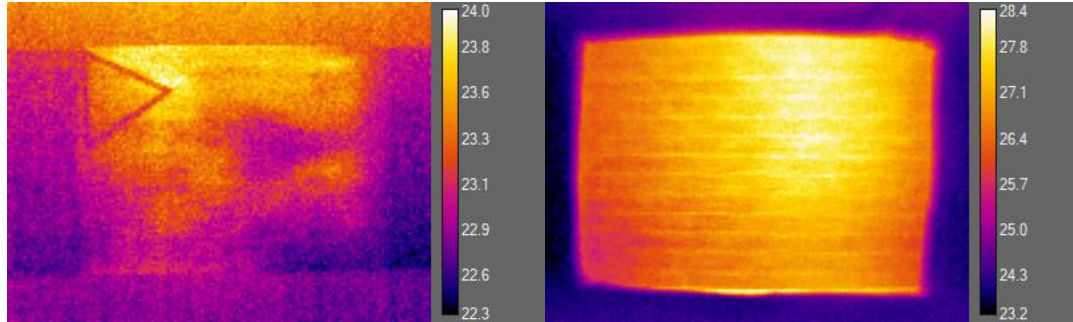


Figure 50: 3wt% ACNT ZTCFRP 4p: at 8.13s (JH-IRT) and at 59.33s (F-IRT).

## **4.3 Defect analysis**

### **4.3.1 Electrical resistivities of bond-line resins with 4-probe measurement**

The resulting conductivities were inaccurate in contrast to the preliminary study. This unevenness in data can be summarized by a few things. When the measurement tool was cured inside a vacuum oven for two hours at 120°C, sometimes the tool became warped and could shift the delicate wires within the tool which possibly obscured the measurement.

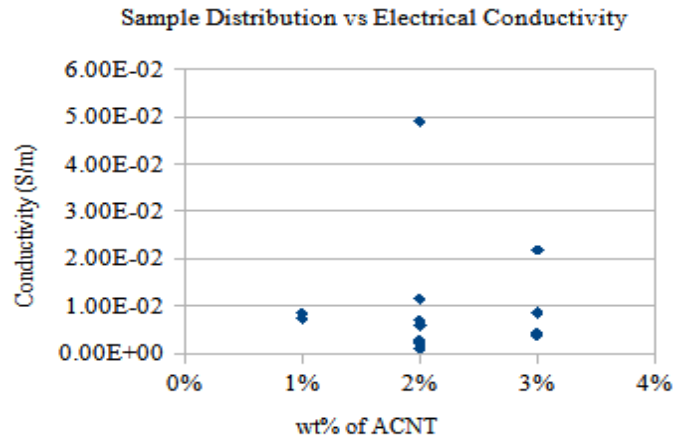


Figure 51: 4 probe bond-line resistivity results.

Several samples to determine the Tt.E.C. were conducted using the 4 -probe resistivity tool in Figure 27. Some of these values have a large coefficient of variation.

#### 4.3.2 Defect area similarity parameter

As stated in section 3.4, the defect visible from the thermograms above divided by the defect template area can characterize the differences in ply count and wt% of ACNT. The outcome from these measurements have shown that the defect area is not always larger than the template. This is more apparent in the ply # experiments where both CCFRP and ZTCFRP display a smaller defect area than the template. Another observation was the decrease in difference from the template area as the wt% of ACNT increased for the ZTCFRP cases. However, the same cannot be said for the CCFRP cases. To avoid issues with defect similarity values being more than the template, the absolute variation from the template was used for the grading criteria.

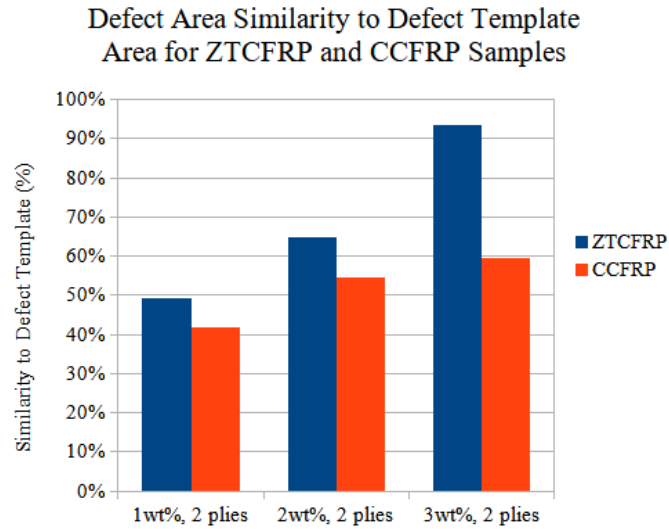


Figure 52: Defect area similarity for samples of two plied ZTCFRP and CCFRP (JH-IRT).

In Figure 52 the trend shows that, regardless of wt% of ACNT, ZTCFRP outperforms CCFRP for defect area similarity. This indicates that the wt% of ACNT does not have as much an impact on the defect area similarity for CCFRP. Furthermore, the ZTCFRP samples increase in performance as the wt% of ACNT is increased. This shows that the nanostructure of the CNF within the ZTCFRP meshes well with the conductive resin bond-line.



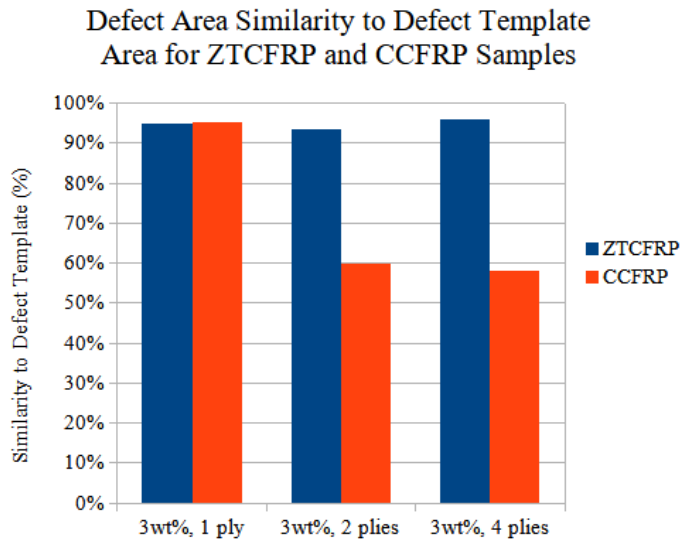


Figure 53: Defect area similarity for ZTCFRP and CCFRP of various ply thicknesses (JH-IRT).

The defect area similarity with respect to the number of plies of ZTCFRP and CCFRP shows that ZTCFRP is not negatively affected as much as the CCFRP. The overall trend for CCFRP shows a steep decline in visual clarity for the defect area as the number of plies increases. This is to be expected as the insulative properties of neat epoxy within the CCFRP becomes more apparent as the number of plies increases. This is in stark contrast to the trend ZTCFRP exhibits. Like the trend in Figure 52, ZTCFRP seems to be independent of the number of plies in terms of the defect area similarity. In both cases, ZTCFRP outperforms CCFRP in terms of the defect area similarity, as it benefits from a higher wt% of ACNT which would otherwise be wasted on CCFRP.

### 4.3.3 Defect shape similarity parameter

The shape of the defect with respect to the ACNT wt% experiment did not seem to have a clear trend. The ply number experiment showed that the defect was closer to its original shape starting from one ply thick before dropping in its fidelity. It is interesting to observe that both ZTCFRP and CCFRP samples almost reached a perfect match. This is possibly due to the very conductive bond-line allowing the finer details such as sharper corners stand out in the thermogram. In each case, for the fixed wt% experiment, the ZTCFRP samples outperform the CCFRP samples.

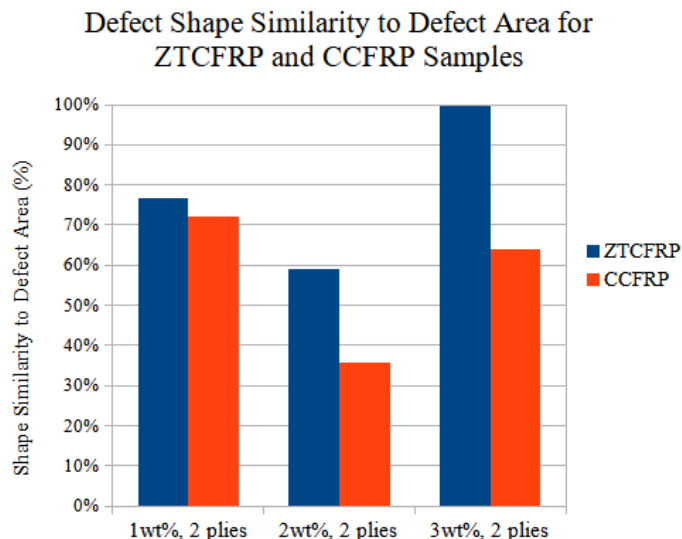


Figure 54: Shape similarity of ZTCFRP and CCFRP bonded to various wt% ACNT (JH-IRT).

Much like the defect area similarity, a higher wt% of ACNT correlates with higher similarity of the defect area to its true shape, at least for ZTCFRP. The shape

similarity of CCFRP seems inferior to ZTCFRP, regardless of the wt% of ACNT.

Additionally, the 2wt% two ply case for ZTCFRP was less than an ideal test sample in which air pockets were trapped within the ZTCFRP variant and can be seen undergoing F-IRT in Figure 47 as cold spots in the bond-line area.

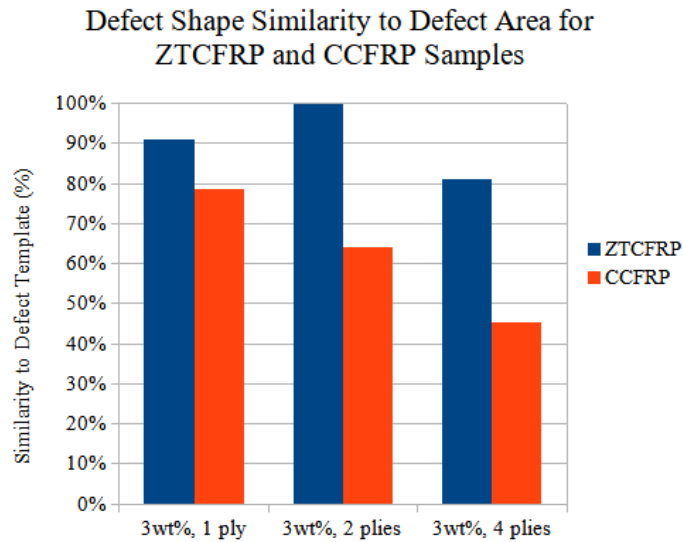


Figure 55: Shape similarity of ZTCFRP and CCFRP of various ply thicknesses (JH-IRT).

This trend in the figures above indicates that the smaller ply count correlates with a greater defect shape similarity. The trend between ZTCFRP and CCFRP share the same ACNT wt%, but vary in thickness, look very similar to each other but differ in scale. Figure 55 above shows a very clear trend where ZTCFRP and CCFRP's defect shape similarity degrades as the number of plies thick increases. Yet, ZTCFRP outperforms CCFRP with a difference in range of ~19% compared to ~34% for CCFRP.

### 4.3.4 Final defect grading

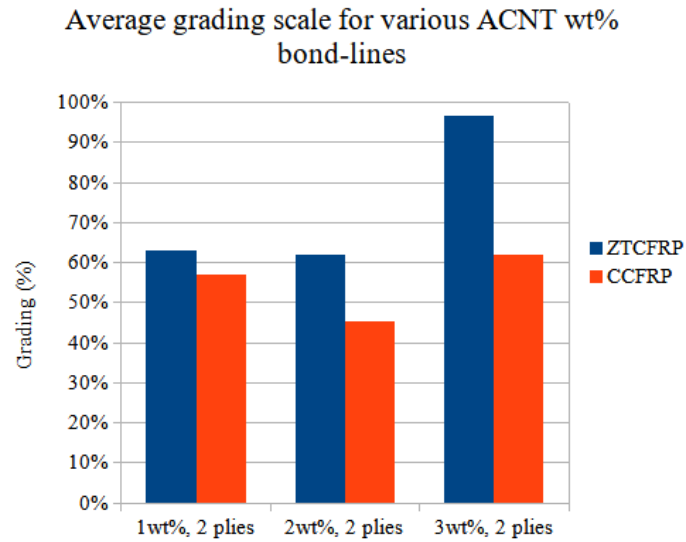


Figure 56: Average grading of ZTCFRP and CCFRP with various wt% ACNT (JH-IRT).

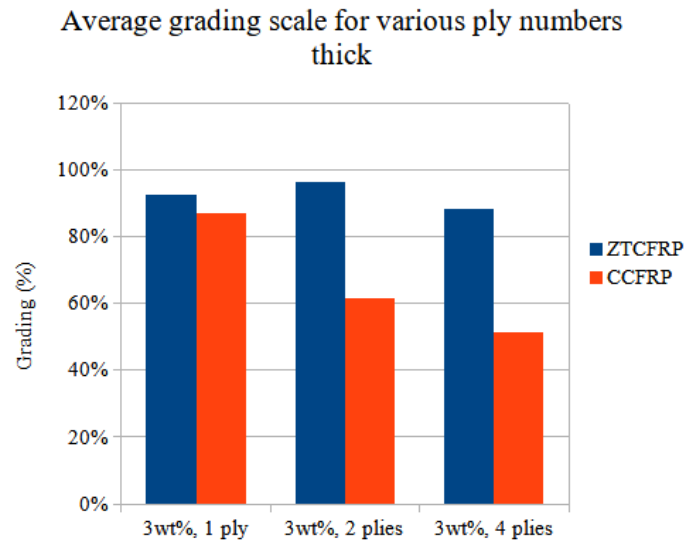


Figure 57: Average grading of ZTCFRP and CCFRP with various ply thicknesses (JH-IRT).

ZTCFRP outperforms CCFRP in every case, both in parameter and average grading.

#### 4.3.5 Defect quality improvement of ZTCFRP over CCFRP

A more direct comparison can be made when comparing the values from both CFRP systems in terms of area similarity and shape similarity to each other. The values listed below were calculated using the equation below.

$$Improvement_{Area\%} = \left( \frac{Defect\ area\ similarity_{ZTCFRP\ Case}}{Defect\ area\ similarity_{Control\ Case}} \right) - 1 \quad (11)$$

$$Improvement_{Shape\%} = \left( \frac{Shape\ similarity_{ZTCFRP\ Case}}{Shape\ similarity_{Control\ Case}} \right) - 1 \quad (12)$$

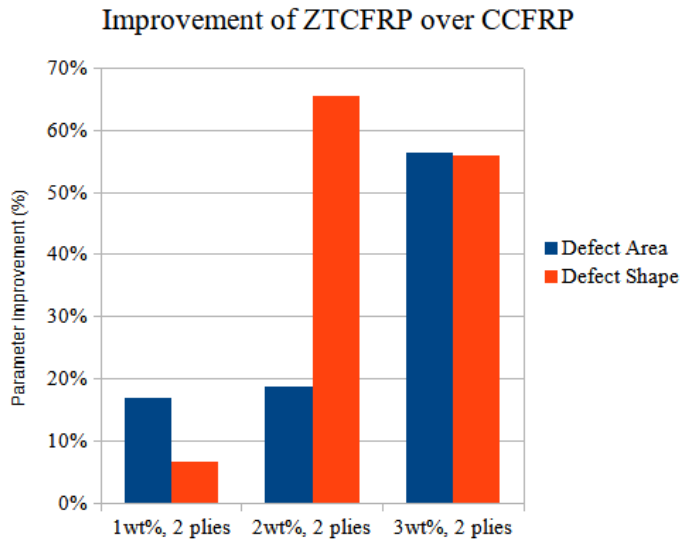


Figure 58: Improvement of ZTCFRP over CCFRP with various wt% ACNT (JH-IRT).

The percentage of improvement of the defect area and defect shape parameter between both CFRP systems are all in favor of ZTCFRP with the exception of the 3wt

ACNT one ply case where the CCFRP sample's defect area is slightly greater than ZTCFRP with a score of -0.68%. The trend of defect area similarity for ZTCFRP is a clear increase in clarity as the wt% of ACNT increases inside the bond-line. The same is true for defect shape similarity although the trend is more chaotic. The large improvement in the defect shape similarity for the 2wt% two plied case in favor to ZTCFRP can be better visualized by viewing Figures 41 and 47 and the shapes for ZTCFRP and CCFRP.

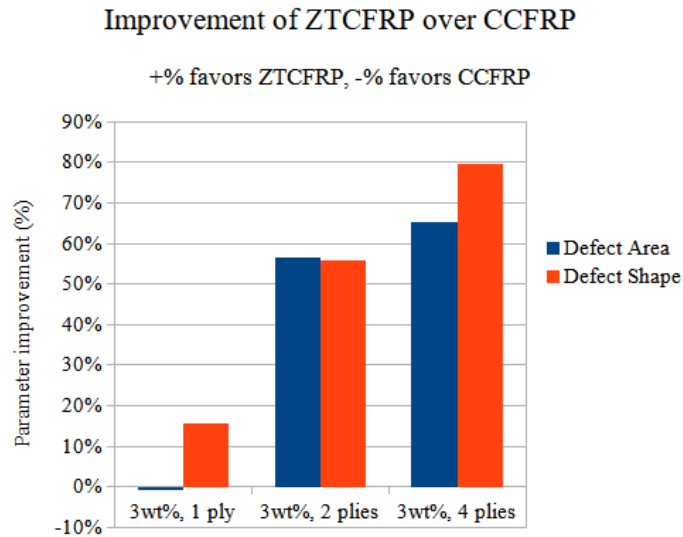


Figure 59: Improvement of ZTCFRP over CCFRP with various ply thicknesses (JH-IRT).

The 3wt% ACNT one ply case has nearly equal values for the defect area similarity between both ZTCFRP and CCFRP. This is to be expected since with only a lamina thick per coupon, the heat diffuses much easier through the bond-line and the differences in ZTCFRP and CCFRP become less apparent. This is in stark contrast to the 3wt% ACNT four ply case as the area similarity has nearly an 80% lead over CCFRP. An

interesting thing to note is how the number of plies influences the two parameters. The trend of improvement is in favor of ZTCFRP for both parameters. As the number of plies in thickness increases, ZTCFRP effectiveness for displaying the parameters increases as CCFRP stagnates. This is evident in Figure 57 where the average grades of the ZTCFRP cases have a difference in range of approximately 8% in contrast to approximately 36% for the CCFRP cases as the heat flows through the bond-line, the chance of the shape of the defect becoming softer at the edges increases with the number of plies. In either case, the trend above clearly shows a clearer, more well-defined defect is seen using ZTCFRP over CCFRP. The only caveat to this is the shape similarity for the 2wt% ACNT two ply case where the CCFRP variant has advantage over the ZTCFRP. This is true, although not by fault of the ZTCFRP. In Figure 32, air pockets are positioned very close to the defect which resulted in an obscured shape similarity value. This case acts as the outlier for this trend of improvement. Had there been another sample with air pockets absent this would most likely result in a higher shape similarity value in favor of the ZTCFRP, further strengthening the emerging trend.

#### **4.3.6 Direct comparison of JH-IRT and F-IRT methods**

Drawing comparisons between two different types of active thermography can be challenging, but in this case, there is a concise parameter that distinguishes which method is superior in characterizing defects within a CCFRP/ZTCFRP bond: the useful time to view the defect. This parameter can be viewed independently. It is very short for F-IRT while longer for JH-IRT, which can sustain a visible defect image for the full duration of the recording. Effort into characterizing the shape and defect area similarity values for F-IRT was used to further substantiate the results. However, due to an inconsistent defect

response when the samples undergo F-IRT, this would only provide a very fragmented understanding when comparing with JH-IRT.

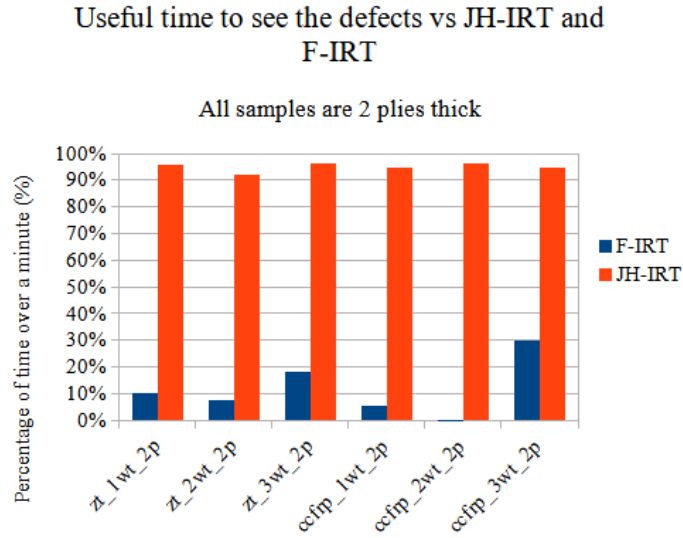


Figure 60: Comparing useful defect time for IRT cases of various ACNT wt%.

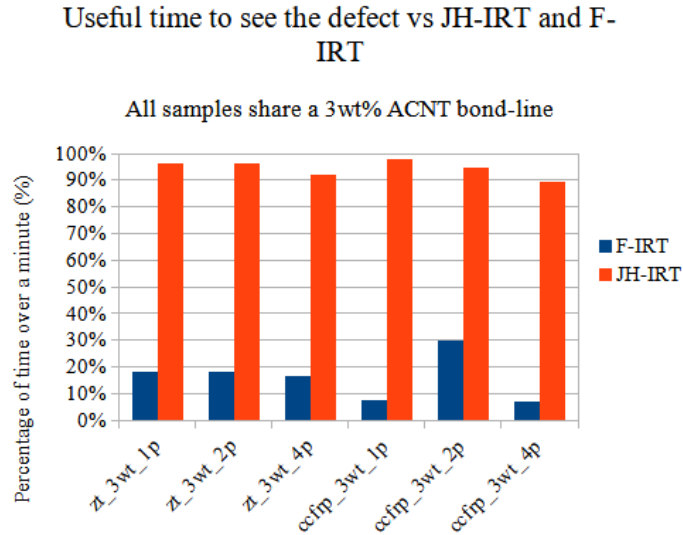


Figure 61: Comparing useful defect time for both IRT cases with various ply thicknesses.



## **CHAPTER V**

### **DISCUSSION**

The comparison between the JH-IRT and F-IRT methods in this study has yielded insight into which types of defects can be seen within the bond-line area. As shown in the F-IRT experiment, the dark regions within the bond-line area signified air pockets trapped inside the resin bond. This is apparent as these regions linger as the rest of the bond-line warms more or less homogenously when undergoing the flash heating method. However, the intentional defects did not stand out as well as the JH-IRT method. This contrast in method effectiveness is further demonstrated when it comes to the useful time to view the defect. The JH-IRT technique, in all cases except the control bond-line samples, yielded defect images which lasted the majority of the recording time. With the flash technique, this time span was either very short or not measurable due to the absence of the defect appearing for some cases. Additionally, the defect regions' mean temperature and the mean bond-line temperature at the flash heating method's best frame was very slight and nowhere near the contrast given by the JH-IRT method. Although JH-IRT was by far the most effective way to see the defect images, the information given from the flash heating method was still useful with the locations of the air pockets known. This raises questions regarding how the discrepancies in the bond-line structure could affect the grading scale for the cases.

The formation of air pockets was a disappointing outcome for testing, although through flash heating, this limited the criticism in grading for the samples most affected by them. The grading criteria has been changed much over the course of this study. It was originally concerned with the apparent area cast by the defect with respect to the template yet expanded to include the aspects of shape, user practicality, power applied, and temperature gradient. The useful time criteria was also changed throughout the study, which first meant the difference in time between the best defect frame and the frame where the defect first emerged then divided by the total time of the recording. This was changed to the time of seeing the defect as a whole divided by the total time of recording or until the defect reached its surroundings temperature. In future works, this parameter could be changed to include the change in defect area from the best frame to the last frame to characterize the defect image.

The grading formula was also changed to a more unbiased comparison for the cases. This was done by taking the values of each parameter ratio and then normalizing it to a 0 and 1 scale. This would effectively make each parameter the same weight of importance to the technician. This worked on paper but had issues in practice. For instance, the useful time for 3wt% ACNT with one CCFRP ply thickness compared to 3wt% ACNT with four CCFRP ply thickness would be vastly different as the 3wt% ACNT with one CCFRP ply sample. This comparison shows the one-ply thick sample would reach its best frame much quicker than the four-ply sample. This would result in a lower useful time value and make the one-ply sample appear less attractive than the four-ply sample. This was another reason to change the useful time parameter as explained above. This parameter seems trivial with the JH-IRT thermography samples as each of

the cases, except for control, would have very similar values. However, the flash heating thermography useful times vary much more, which gives more influence over the final grading. The final grading scale was changed to simplify the grading criteria. The defect area similarity and shape similarity values for each case were averaged and then listed as a percentage.

Lessons learned from manufacturing the test samples were more plentiful in this thesis as many of the past manufacturing decisions from the preliminary study clashed with the testing procedures in the investigative study. While some aspects of the overall procedure would be changed to acclimatize to the inclusion of ZTCFRP, the CF could not. Changing the CF from T700s to another CF system more easily manufactured, like the lower areal weight fabric of AS4 or AS7, would discredit the entirety of the preliminary study which would then need to be conducted again with the chosen CF. Impregnating the 680 GSM high areal weight of T700S CF would take months of resin, temperature, and procedure tweaking to make a viable prepreg. The trade for making ZTCFRP with T700s was a reduction in FVF as well as impregnation depth which was a very time intensive tuning to have repeatable prepreg quality.

Regarding the investigative results, it seems that ZTCFRP did well against CCFRP in the ply number experiment in examining the shape similarity as the scoring was always more than the CCFRP values. This is in agreement with the findings where ZTCFRP was able to maintain a defect area and shape similar to the copper triangle underneath it compared to the CCFRP variant where the defect shape was elongated and larger in area. This is thought to be the case as the CF was unidirectional so the thermal conductivity in the through-thickness direction was blocked due to the resin matrix. The

ZTCFRP enhanced the Tt.T.C. inside the resin matrix which allowed heat to flow more easily without disrupting the shape. The results of the shape similarity with regards to the various wt% of ACNT was less definite as the two plied 2wt% ACNT ZTCFRP had a larger and less defined defect shape due to air pockets trapped near the defect as seen in Figure 47. The trend where the ZTCFRP samples surpass CCFRP is more agreeable with 1wt% and 3wt% ZTCFRP samples outperforming their CCFRP counterparts.

The defect area similarity results show that ZTCFRP is best when compared to CCFRP for the various wt% of ACNT in Figure 52. The results for the ply number experiment in regard to defect area similarity show that the differences in ZTCFRP and CCFRP are less apparent as both score high and closely to each other. This is not indicative of describing the entire trend of increasing the number of plies to the samples because ZTCFRP continues to outperform CCFRP.

## **CHAPTER VI**

### **CONCLUSIONS**

After the investigative study it seems that ZTCFRP and CCFRP, to some extents, are viable mediums for JH-IRT. The conductive bond-lines have shown that 3wt% ACNT is the most consistent at displaying the defect image regardless of the number of plies. The shape and defect similarity parameters have been a good litmus test to characterize many aspects of the defect image at a given time. In the comparison between JH-IRT and F-IRT, JH-IRT performs approximately 842% better than that of F-IRT in terms of useful defect time with a standard deviation of 475% and a COV of 56.3%.

For future works, a more robust grading scale could better characterize defect images. One approach would be to implement a more robust shape determination technique for defects not triangular in shape. Another way to enhance what was built over this study would be to introduce more image analysis in terms of temperature gradient. Converting a colored image into grey scale could be a useful technique. However, the technicalities of this approach are harsh, as finding the best way to threshold the image to display the greatest contrast every single time would require many working algorithms to run at the same time and then pick the best result.

Another lesson learned was to appreciate the complexity of a system even if the tools used to describe it are simple in nature. If time permitted, the measured temperature

gradient would be included into the final scoring. The data is already available, though implementing it in an easy to digest manner has been difficult to implement. This is evident as each length between the hot and cold regions near the defect would be different for every sample and would result in inconsistent measurements and an inability to form a coherent trend. Work into the changes in the COV for the bond-line throughout the JH-IRT procedure has been considered. However, including this into the final grading would be trivial as each sample and their bond-lines must be almost exactly the same as the variance in the current data would result in inconsistent trends. This is compounded by considering the presence of air pockets trapped inside the bond-line, surface sanding conditions, uniformity of bond-line Tt.E.C., uniformity of Tt.T.C., the initial temperature, as well as the fact that many other properties of the composites would need to be very similar. However, this idea sounds feasible as if a defect is present while undergoing JH, the heat would irregularly travel through the bond-line as seen in this study. The variance from the defect area mean temperature and bond-line mean temperature would steadily increase as it is heated through JH. The resulting COV would register the difference in temperature and can be plotted.

The direct comparison between ZTCFRP and CCFRP provided great insight into which CFRP system would promote clean and accurate defect images. As far as the defect similarity parameter is concerned, ZTCFRP had a 17.02% improvement for 1wt% ACNT two plies thick, 18.79% for 2wt% ACNT two plies thick, 56.43% for 3wt% ACNT two plies thick, -0.68% for 3wt% ACNT one ply thick, and 65.20% for 3wt% ACNT four plies thick improvement over CCFRP. For the shape similarity parameter, 6.63% for 1wt% ACNT two plies thick, 65.48% for 2wt% ACNT two plies thick, 55.86%

for 3wt% ACNT two plies thick, 15.72% for 3wt% ACNT one plies thick, and 79.65% for 3wt% ACNT four plies thick improvement over CCFRP.

The findings from this study have shown that ZTCFRP composites perform well in characterizing the shape and area of internal defects within a conductive adhesive bond-line. This is not to imply that its challenger, CCFRP, is not effective in these respects. In actuality, both CFRP systems perform admirably in the JH-IRT procedure, but ZTCFRP is more effective in displaying these parameters. Future studies could further improve the current understanding by creating better quality bond-line resins infused with ACNT without damaging the nanostructure, by characterizing irregularly shaped defects with the same precision or more than what this study accomplished, and by showing more comparisons to NDE methods other than F-IRT. Electrical impedance tomography or pulsed thermography or eddy current thermography could work well given the in-situ properties of ZTCFRP and the conductive bond-line resin matrices.

## REFERENCES

1. Budhe, S., Banea, M. D., de Barros, S., & da Silva, L. F. M. (2017). An updated review of adhesively bonded joints in composite materials. *International Journal of Adhesion and Adhesives*, 72, 30–42. <https://doi.org/10.1016/j.ijadhadh.2016.10.010>
2. Grand View Research. (n.d.) Carbon Fiber Market Size & Share: Industry Growth Report, 2018-2025. In Grand View Research. Retrieved July 29, 2022, from <https://www.grandviewresearch.com/industryanalysis/carbon-fiber-market-analysis> .
3. Hsiao, K. T., Alms, J., & Advani, S. G. (2003). Use of epoxy/multiwalled carbon nanotubes as adhesives to join graphite fibre reinforced polymer composites. *Nanotechnology*, 14(7), 791.
4. Taylor, W. W., Uddin, M. N., Islam, M. R., Dizbay-Onat, M., & Hsiao, K. T. (2022, May 23-26). *A Preliminary Study of Using Film Adhesives Containing Aligned and Unaligned Nanotubes and Nanofibers for Bonding CFRP Laminates and Steel Plates* [Conference presentation]. SAMPE 2022 Conference Proceedings, Charlotte, NC. Retrieved from <https://par.nsf.gov/biblio/10386694>.
5. Kumar, V., Yokozeki, T., Karch, C., Hassen, A. A., Hershey, C. J., Kim, S., ... & Kunc, V. (2020). Factors affecting direct lightning strike damage to fiber reinforced composites: A review. *Composites Part B: Engineering*, 183.



6. Heslehurst, R. B. (2014). *Defects and damage in composite materials and structures*. CRC press.
7. Baltopoulos, A., Polydorides, N., Pambaguian, L., Vavouliotis, A., & Kostopoulos, V. (2013). Damage identification in carbon fiber reinforced polymer plates using electrical resistance tomography mapping. *Journal of composite materials*, 47(26), 3285-3301.
8. Schueler, R., Joshi, S. P., & Schulte, K. (2001). Damage detection in CFRP by electrical conductivity mapping. *Composites science and technology*, 61(6), 921-930.
9. Mallick, P. K. (2007). *Fiber-reinforced composites: materials, manufacturing, and design*. CRC press.
10. Gholizadeh, S. (2016). A review of non-destructive testing methods of composite materials. *Procedia structural integrity*, 1, 50-57.
11. Usamentiaga, R., Venegas, P., Guerediaga, J., Vega, L., Molleda, J., & Bulnes, F. G. (2014). Infrared thermography for temperature measurement and non-destructive testing. *Sensors*, 14(7), 12305-12348.
12. Suzuki, Y., Todoroki, A., Matsuzaki, R., & Mizutani, Y. (2012). Impact-damage visualization in CFRP by resistive heating: Development of a new detection method for indentations caused by impact loads. *Composites Part A: Applied Science and Manufacturing*, 43(1), 53-64.
13. Chrysafi, A. P., Athanasopoulos, N., & Siakavellas, N. J. (2017). Damage detection on composite materials with active thermography and digital image processing. *International journal of thermal sciences*, 116, 242-253.

14. Han, J.H., Zhang, H., Chen, M.J., Wang, D., Liu, Q., Wu, Q.L., & Zhang, Z. (2015). The combination of carbon nanotube buckypaper and insulating adhesive for lightning strike protection of the carbon fiber/epoxy laminates. *Carbon*, 94,101–13. <https://doi.org/10.1016/j.carbon.2015.06.026>.
15. Kumar, V., Yokozeki, T., Okada, T., Hirano, Y., Goto, T., Takahashi, T., & Ogasawara, T. (2018). Effect of through-thickness electrical conductivity of CFRPs on lightning strike damages. *Composites Part A: Applied Science and Manufacturing*, 114, 429-438.
16. Li, C., Thostenson, E. T., & Chou, T. W. (2007). Dominant role of tunneling resistance in the electrical conductivity of carbon nanotube–based composites. *Applied Physics Letters*, 91(22).
17. Bal, S. (2010). Experimental study of mechanical and electrical properties of carbon nanofiber/epoxy composites. *Materials & Design (1980-2015)*, 31(5), 2406-2413.
18. Ranabhat, B., & Hsiao, K. T. (2018). Improve the through-thickness electrical conductivity of CFRP laminate using flow-aligned carbon nanofiber z-threads. *International SAMPE Symposium and Exhibition*. <https://par.nsf.gov/biblio/10075362>.
19. Scruggs, A. M., Kirmse, S., & Hsiao, K. T. (2019). Enhancement of Through-Thickness Thermal Transport in Unidirectional Carbon Fiber Reinforced Plastic Laminates due to the Synergetic Role of Carbon Nanofiber Z-Threads. *Journal of Nanomaterials*, 2019.
20. Salim, M. U., Nishat, F. M., Oh, T., Yoo, D. Y., Song, Y., Ozbakkaloglu, T., & Yeon, J. H. (2022). Electrical Resistivity and Joule Heating Characteristics of Cementitious

- Composites Incorporating Multi-Walled Carbon Nanotubes and Carbon Fibers. *Materials*, 15(22), 8055.
21. Enoki, S., Moriito, K., Tanaka, K., & Katayama, T. (2014). CFRTP molding method of the three-dimensional shape by using direct resistance heating to carbon fiber. *High Perform. Opt. Des. Struct. Mater*, 137, 273-287.
  22. Sung, P. C., & Chang, S. C. (2015). The adhesive bonding with buckypaper–carbon nanotube/epoxy composite adhesives cured by Joule heating. *Carbon*, 91, 215-223.
  23. Loos, M. (2015). Fundamentals of polymer matrix composites containing CNTs. *Carbon nanotube reinforced composites*, 125-170.
  24. Rahman, M., Schott, N. R., & Sadhu, L. K. (2016). Glass transition of ABS in 3D printing. *COMSOL Conference, Boston, MA*.
  25. Singh, N., & Singh, R. (2017). Conducting Polymer Solution and Gel Processing. Reference Module in Materials Science and Materials Engineering, Elsevier, 2017. <https://doi.org/10.1016/B978-0-12-803581-8.03733-4>.
  26. Bell, Terence. (2021, August 3). Electrical Conductivity of Metals. Retrieved from <https://www.thoughtco.com/electrical-conductivity-in-metals-2340117>
  27. Lanc, Z., Zeljković, M., Štrbac, B., Živković, A., Drstvenšek, I., & Hadžistević, M. (2015). The determination of the emissivity of aluminum alloy AW 6082 using infrared thermography. *J. Prod. Eng.*, 18, 23-26.
  28. Collinson, M., Hayes, S., & Petropoulos, S. (2020). The effect of type of mechanical processing on electrical conductivity and piezoresistive response of CNT and graphite composites. *Procedia CIRP*, 85, 311–317.

29. Hsiao, K.T. “Novel liquid matrix impregnation method and apparatus for composite prepreg production.” U.S. Patent WO2022221521A1, October 20<sup>th</sup>, 2022. Available online: <https://patents.google.com/patent/WO2022221521A1/en>.
30. Loh, K., & Nagarajaiah, S. (2016). *Innovative developments of advanced multifunctional nanocomposites in civil and structural engineering*. Woodhead Publishing.
31. McAndrew, T. P., Havel, M., Korzhenko, A., & Delprat, P. (2013). Composites with Multi-Walled Carbon Nanotubes. *Arkema Inc, 900*.

## APPENDICES

### Appendix A: Preliminary study

Table A1. Preliminary IRT results.

Case	Average Resistance (Ohm)	Voltage (V)	Current (Amps)	Power (W)	Best Frame Time (s)	Visual Quality (1-6) (1=Best) (6=Worst)
0.8 wt% CNF	77.52	5.00	0.76	3.80	8.00	5
2 wt% CNF	21.89	5.00	0.27	1.33	61.00	4
3 wt% CNF	18.27	5.00	0.29	1.47	11.00	2
4 wt% CNF	12.47	5.00	0.44	2.22	76.00	5
0.8 wt% ACNT	792.12	5.00	0.01	0.04	38.00	6
2 wt% ACNT	49.93	5.00	0.17	0.83	24.00	3
3 wt% ACNT	7.51	5.00	0.85	4.20	9.00	2
4 wt% ACNT	7.62	5.00	1.00	5.00	7.00	1
Average	123.41	5.00	0.47	2.36	29.75	
Stdev	271.29	0.00	0.35	1.77	26.69	
COV	219.81%	0.00%	75.02%	75.12%	91.26%	
Min	7.51	5.00	0.01	0.04	7.00	
Max	792.12	5.00	1.00	5.00	76.00	

Table A2. Testing sample dimensions and Tt.E.C. for various ACNT, and CNF wt%<sub>s</sub>.

Film Adhesive Type	Wt% of nanofiller	Average Bonding Area (cm <sup>2</sup> )	Average Bond-line thickness (mm)	Average Tt.E.C. (S/m)	COV of Tt.E.C. (%)	Improvement over 0.8wt% CNT and CNF
CNT	1.00	57.97±1.08	0.885±0.10	2.03e-4	0.00%	0.00%
	2.00	58.32±1.08	0.701±0.10	2.37e-3	0.60%	1064%
	3.00	58.28±1.08	0.914±0.10	2.14e-2	5.0%	10435%
	4.00	60.86±1.10	0.754±0.10	1.64e-2	2.50%	7950%
CNF	0.80	56.75±1.07	0.723±0.10	1.61e-3	0.50%	0.00%
	2.00	59.59±1.09	0.870±0.10	6.83e-3	1.80%	323%
	3.00	58.21±1.08	0.889±0.10	8.62e-3	1.10%	434%
	4.00	55.78±1.06	0.794±0.10	1.20e-2	2.90%	641%
	Average	58.22	0.816	0.56		
	Stdev	1.56	0.08	0.05		
	COV	2.68%	10.23%	8.23%		
	Min	55.78	0.70	0.51		
	Max	60.86	0.914	0.68		

## Appendix B: Investigative study

### **B1. Methodology of characterizing the best defect frames using ResearchIR**

This part of the investigative study deserves more context into how the best defect frame in every case was chosen as well as the resulting parameter measurements.

Following the setup displayed in Figure B1, the bond-line sample undergoes JH-IRT, and video data was recorded as a sequence file for ResearchIR to analysis. The recording consisted of 900 frames over the course of a minute, or 15 frames per second (FPS).

Because the push of the recording and output buttons happened simultaneously, adjustments to the starting time and the onset of current were not calculated. If the recording began five seconds before or after the current was imposed, this would need to be taken into account which was done so for the flash heating measurements. Due to the CCFRP and ZTCFRP being thermally conductive as stated earlier, ample time was given between the last contact of securing the test sample in place prior to measurement and the start of the measurement. This span of time was from 10-15 minutes to allow the sample to reach the room temperature as closely as possible ( $22^{\circ}\text{C}$ ). The maximum temperature prior to recording was restricted to between  $23^{\circ}\text{C}$  and  $24^{\circ}\text{C}$ .

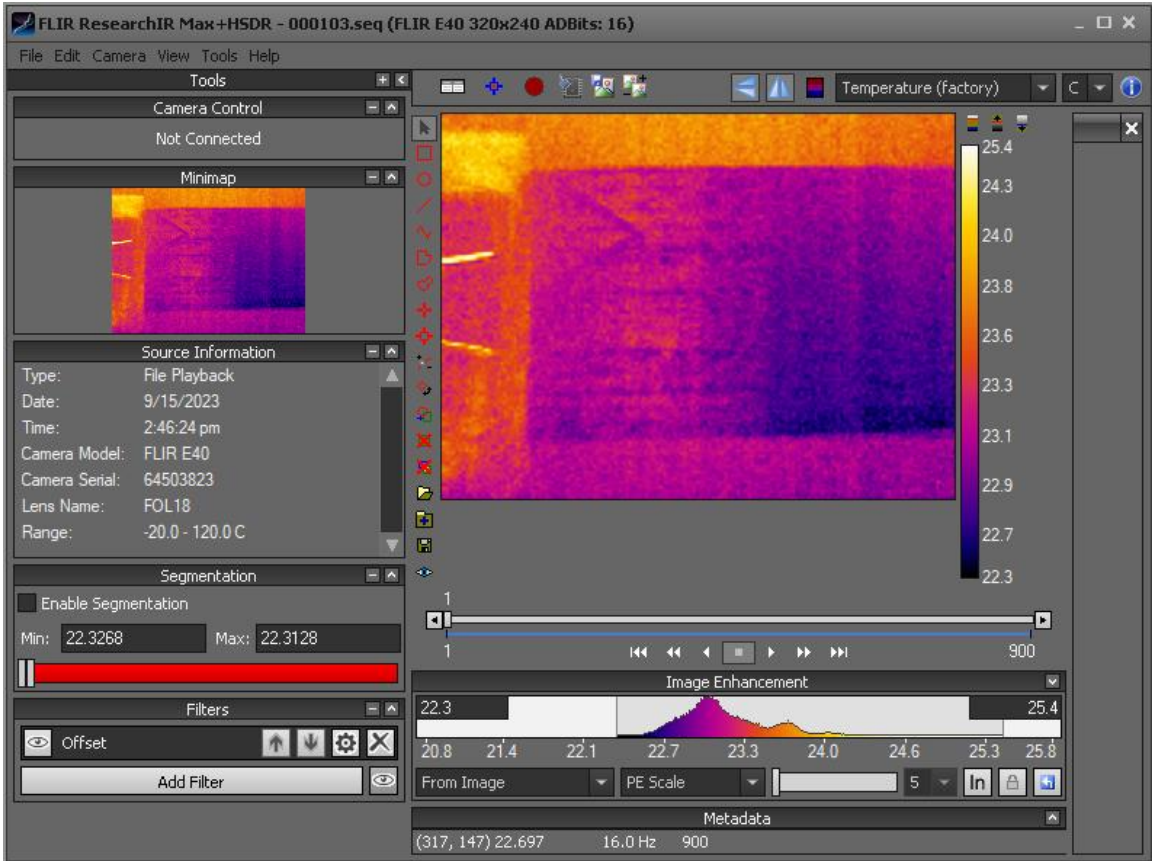


Figure B1. ResearchIR user interface.

Once the data was recorded, the sequence file was uploaded into the ResearchIR user interface. Many things could be done at that point to manipulate the starting conditions to reflect a consistent starting point for each of the tests. The initial frame's minimum temperature was 'locked' in place to function as the lower bound for the temperature range. The last frame's maximum temperature, or the maximum temperature for the whole recording was set as the upper bound for the temperature range. Once this was done, the temperature scale was offset by the initial minimum temperature. The best frame was based on a visual inspection of the thermogram frames where the area cast by the defect and the overall shape of that area were considered most closely related to the



defect template. Once that frame was chosen, it was recorded as the best frame (BF) for that case.

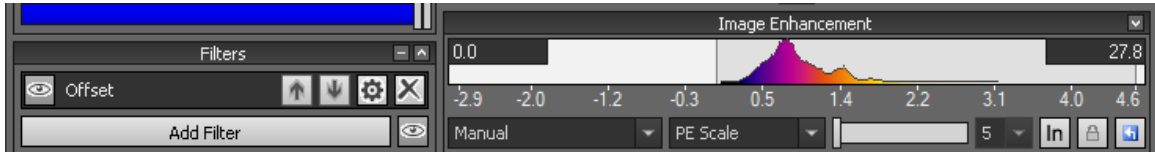


Figure B2. Offset and fixed temperature range implementation.

After the BF is found, the thermogram was exported as a portable network graphic (PNG) image and then placed into its respective file with its directory name listing the ACNT wt%, the CFRP systems, the ply number, the frame number, and the IRT method used.

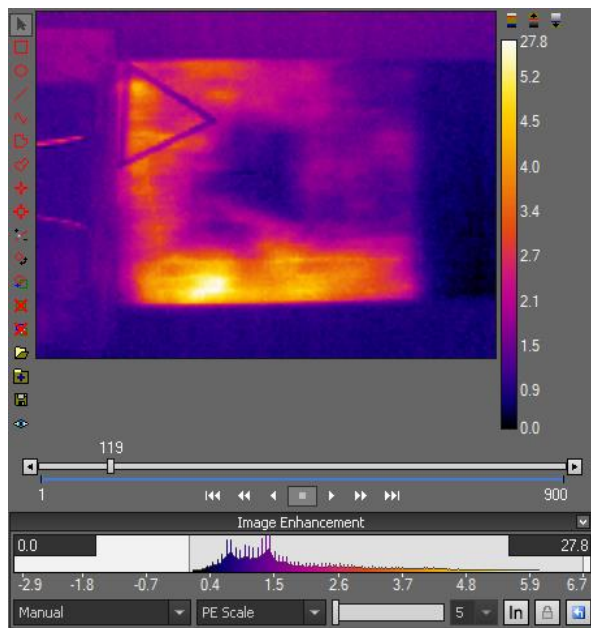


Figure B3. BF for test sample 3wt% ACNT ZTCFRP 1ply, (JH-IRT).

This PNG file was imported to another software called ImageJ which was used for image analysis and post-processing. ImageJ had a function to place a uniform grid onto an image which was useful in calculating the defect area and the shape similarity.

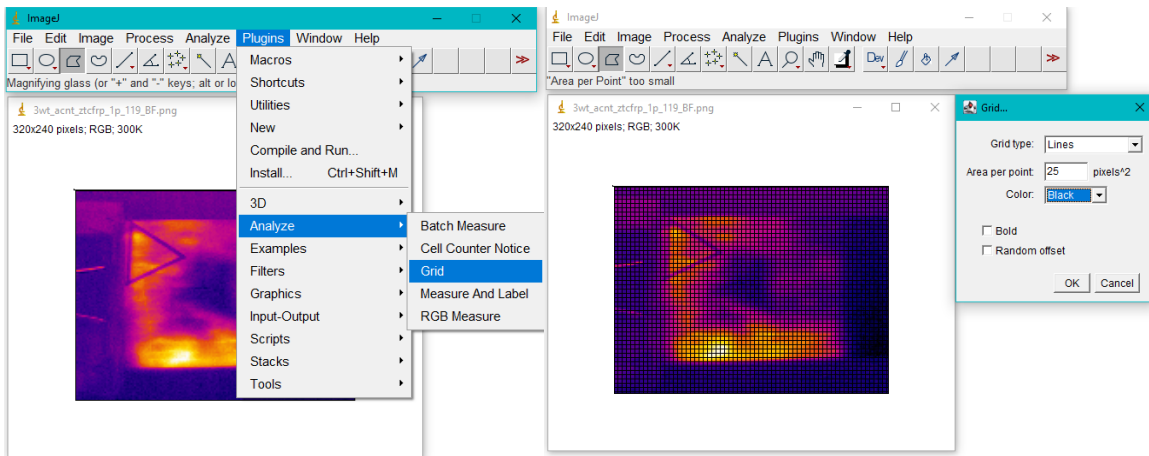


Figure B4. Placing the grid overlay onto the thermogram.

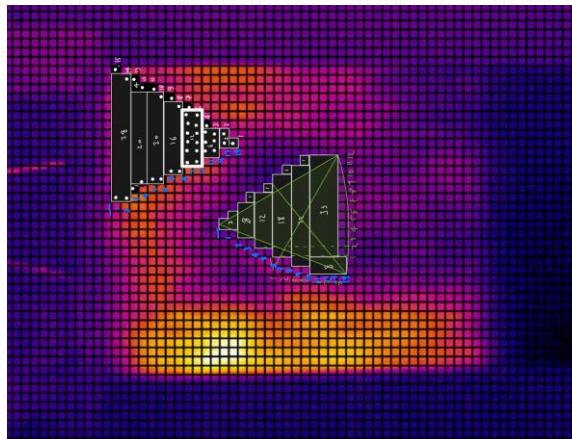


Figure B5. The resulting defect area and shape similarity estimation.

Notice the green lines on the defect area signify the median lines used in the shape similarity parameter equation. If the median lines were not aligned with the grid, their length was estimated using the Pythagorean theorem using whole units.

## **B2. Investigative thermal conductivity**

From section 2.4.1 the equations listed were used to calculate the estimated thermal conductivity for each of the CCFRP and ZTCFRP coupons. The values were taken down after post-cure and before sanding the composites down.

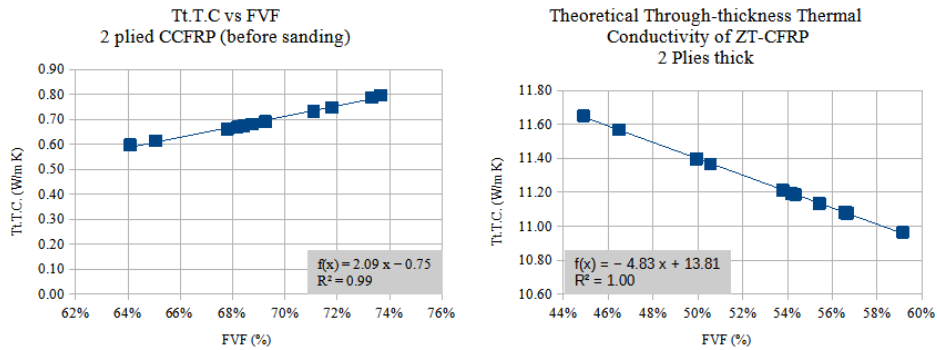


Figure B6. Thermal conductivity estimates for CCFRP and ZTCFRP coupons used for this study. (Left to Right, respectively).

It should be noted that, as the FVF increases, so does thermal conductivity. This was to be expected as a higher FVF means there was less epoxy acting as an insulator between the CF plies.

### B3. Investigative test sample characteristics

Table B1. Physical characteristics of investigative test samples.

CFRP Case	Average Coupon FVF	Density (g/cm <sup>3</sup> )	Thermal Conductivity (w/mk)		Unit Average Thickness (mm) (Full thickness)
CCFRP_0wt_2p	64.09%	1.50	0.59		0.54 (1.08)
CCFRP_1wt_2p	64.52%	1.50	0.60		0.53 (1.05)
CCFRP_2wt_2p	57.00%	1.37	0.44		0.55 (1.10)
CCFRP_3wt_1p	54.42%	1.39	0.39		0.55
CCFRP_3wt_2p	68.11%	1.44	0.67		0.54 (1.07)
CCFRP_3wt_4p	64.65%	1.47	0.70		0.54 (2.16)
ZTCFRP_0wt_2p	53.99%	1.47	11.20		0.52 (1.04)
ZTCFRP_1wt_2p	56.97%	1.45	11.14		0.51 (1.02)
ZTCFRP_2wt_2p	54.42%	1.50	11.19		0.59 (1.18)
ZTCFRP_3wt_1p	56.97%	1.30	11.06		0.68
ZTCFRP_3wt_2p	56.01%	1.40	11.11		0.56 (1.12)
ZTCFRP_3wt_4p	43.26%	1.33	11.72		0.60 (2.41)
			CCFRP	ZTCFRP	
Average	57.88%	1.43	0.56	11.24	0.56
Stdev	0.07	0.07	0.12	0.24	0.05
COV	11.55%	4.78%	22.01%	2.16%	8.23%
Min	43.26%	1.30	0.39	11.06	0.51
Max	68.11%	1.50	0.70	11.72	0.68

Table B2. Bond-line characteristics.

Case	Bond-line area ( $cm^2$ )	Bond-line Thickness (mm)
CCFRP_0wt_2p	49.08±0.99	1.08±0.10
CCFRP_1wt_2p	49.48±1.01	1.14±0.10
CCFRP_2wt_2p	47.88±0.99	1.10±0.10
CCFRP_3wt_1p	33.14±0.88	1.13±0.10
CCFRP_3wt_2p	49.78±1.04	1.09±0.10
CCFRP_3wt_4p	49.40±1.00	0.93±0.10
ZTCFRP_0wt_2p	45.12±0.93	1.03±0.10
ZTCFRP_1wt_2p	49.59±1.01	1.15±0.10
ZTCFRP_2wt_2p	49.66±1.03	1.02±0.10
ZTCFRP_3wt_1p	48.89±0.99	1.07±0.10
ZTCFRP_3wt_2p	49.40±1.00	1.23±0.10
ZTCFRP_3wt_4p	48.56±0.99	1.13±0.10
Average	47.58	1.09
Stdev	5.11	0.076
COV	10.73%	7.00%
Min	33.14	1.02
Max	49.78	1.23

Table B3. JH-IRT thermogram results.

Bond-line Case p=plies	Defect Similarity (%)	Shape Similarity (%)	Best Frame Time (s)	Applied Voltage (V)	Applied Current (mA)	Applied Wattage (W)	Heat Flux (W/m <sup>2</sup> )		
0wt%, CCFRP, 2p	NA	NA	NA	0.00	0.00	0.00	0.00		
1wt%, CCFRP, 2p	41.96	72.09	7.93	20.00	257	5.14	1038.89		
2wt%, CCFRP, 2p	54.62	35.68	10.53	25.00	201	5.03	1049.50		
3wt%, CCFRP, 1p	95.38	78.54	3.33	17.00	311	5.29	992.88		
3wt%, CCFRP, 2p	71.26	63.96	12.40	9.00	611	5.50	1104.66		
3wt%, CCFRP, 4p	52.94	45.20	28.0	23.00	216	4.97	1005.67		
0wt%, ZTCFRP, 2p	NA	NA	NA	0.00	0.00	0.00	0.00		
1wt%, ZTCFRP, 2p	49.11	76.87	9.8	21.00	191	4.80	986.69		
2wt%, ZTCFRP, 2p	64.89	59.04	12.93	11.00	455	5.01	1007.99		
3wt%, ZTCFRP, 1p	94.74	90.88	5.33	25.00	191	4.78	976.62		
3wt%, ZTCFRP, 2p	93.33	99.68	7.93	7.00	740	5.18	1048.58		
3wt%, ZTCFRP, 4p	95.79	81.21	8.13	19	249	4.73	974.18		
	Defect Similarity (%)	Shape Similarity (%)				Global			
	CC	ZT	CC	ZT					
Average	61.92%	79.57%	59.09%	81.54%	10.63	17.70	342.2	5.04	1018.57
Stdev	0.20	0.22	0.18	0.15	6.77	6.57	194.86	0.24	41.32
COV	32.22%	26.85%	30.65%	18.85%	63.72%	37.10%	56.94%	4.82%	4.06%
Min	41.96%	49.11%	35.68%	59.04%	3.33	7	191	4.73	974.18
Max	95.38%	95.79%	78.54%	99.68%	12.93	25	740	5.50	1104.66

## BIOGRAPHICAL SKETCH

Name of Author: William W. Taylor

Graduate and Undergraduate Schools Attended:  
The University of South Alabama, Mobile, Alabama, USA

Degrees Awarded:

Master of Science in Mechanical Engineering, 2023

Bachelor of Science in Mechanical Engineering, 2021

Publications:

1. Islam, M. R., Taylor, W., Warren, R., & Hsiao, K.-T. (2023). Enhancing the Interlaminar Shear Strength and Void Control of 3D-Printed Continuous Carbon-Fiber-Reinforced Polymer Composites Using a Robotic Magnetic Compaction Force-Assisted Additive Manufacturing (MCFA-AM) Process and Carbon-Nanofiber Z-Threads. *Applied Sciences*, 13(10), 5914. MDPI AG. Retrieved from <http://dx.doi.org/10.3390/app13105914>.
2. Taylor, W.W., Uddin, N., Dizbay-Onat, M., & Hsiao, K.T. (2022, October 17-20). Non-destructive evaluation (NDE) of bond-line using carbon nanofiber and nanotube modified film adhesive and infrared thermography. *CAMX Conference Proceedings. Anaheim, CA, ()*. Retrieved from <https://par.nsf.gov/biblio/10386716>.

3. Hsiao, K.T., Wu, H., Uddin, Md. N., Hou, Y., Taylor, W.W., & Koo, J.H. (2022, October 17-20). Flammability characterization of carbon nanofibers and nanotubes z-threaded CFRP laminates. *CAMX Conference Proceedings, Anaheim, CA*, (). Retrieved from <https://par.nsf.gov/biblio/10386717>.
4. Taylor, W.W., Uddin, Md. N., Islam, Md. R., Dizbay-Onat, M., & Hsiao, K.T. (2022, May 23-26). A preliminary study of using film adhesives containing aligned and unaligned nanotubes and nanofibers for bonding laminates and steel plates. *SAMPE 2022 Conference Proceedings, Charlotte, NC*, (). Retrieved from <https://par.nsf.gov/biblio/10386694>.
5. Uddin, Md N., Taylor, W.W., Islam, Md R., & Hsiao, K.T. (2022, May 23-26). A preliminary investigation of moisture effect on nanofiber z threaded CFRP prepreg and laminate. *SAMPE 2022 Conference Proceedings, Charlotte, NA*, (). Retrieved from <https://par.nsf.gov/biblio/10386695>.